Dissertation

submitted to the
Combined Faculty for the Natural Sciences and Mathematics
of the Heidelberg University, Germany

for the degree of
Doctor of Natural Sciences

Put forward by

Benedikt Marian Georg Kopp
born in: Vilshofen, Germany

Oral examination: 14.04.2021

New Methods to Evaluate and Reduce Uncertainties in Particle Therapy: From LET Calculation to CICR Planning

Referees: Prof. Dr. Dr. Jürgen Debus

Prof. Dr. Oliver Jäkel

New Methods to Evaluate and Reduce Uncertainties in Particle Therapy: From LET Calculation to CICR Planning

For cancer treatment, particle therapy is becoming increasingly available, featuring precise tumour targeting and favourable depth dose distributions. However, the usage of ionised particles for irradiation is accompanied by a variable and multi-dimensional biological effect. Furthermore, particle therapy is susceptible to range and beam delivery uncertainties. Therefore, new methods and techniques that analyse and mitigate these effects are presented here. To independently verify treatment plans and provide additional clinical insights on relative biological effectiveness (RBE) the FRoG (Fast dose Recalculation on GPU) analytical dose calculation engine has been adapted to a third-party treatment facility and benchmarked. Analyses of a biophysical dose-model that will be used for the first helium-ion therapy with active scanning was carried out, yielding considerable dose-differences for clinically relevant biological assumptions in a biological-sensitivity study. Furthermore, the dose uncertainty of applying a mixed radiation field particle-spectra was quantified, revealing non-negligible but clinically acceptable dose differences. A novel method that combines multiple ion-species in the same treatment field to yield constant RBE, potentially reducing the RBE uncertainty of light ions was developed and experimentally verified in homogeneous and heterogeneous conditions. The investigations presented here contribute to the uncertainty evaluation and reduction of future particle treatments.

Neue Methoden zur Evaluation und Reduktion von Unsicherheiten in Teilchentherapie: Von LET Berechnungen bis CICR Planungen

Teilchentherapie, die sich durch zielgerichtete Bestrahlung und günstige Tiefendosiseffekte auszeichnet, gewinnt zunehmend an Bedeutung für die Krebstherapie. Hinzu kommen jedoch auch variable, multi-dimensionale biologische Effekte und eine Anfälligkeit für Reichweiten- und Bestrahlungsunsicherheiten. Aus diesem Grund werden hier neue Methoden und Techniken vorgestellt, die diese Effekte evaluieren und abschwächen. Um Behandlungspläne unabhängig zu verifizieren und dabei zusätzliche klinische Erkenntnisse über die relative biologische Effektivität (RBE) zu gewinnen, wurde die analytische Dosisberechnungs-Engine FRoG (Fast dose Recalculation on GPU) auf eine weitere behandelndende Klinik angepasst und verifiziert. In einer weiterführenden Studie zur Biosensitivität wurde durch die Analyse eines biophysikalischen Dosismodells, das zur ersten Heliumionenbestrahlung mit aktiv-gelenkter Strahlführung benutzt werden wird, deutliche Dosisunterschiede für zwei klinisch relevante biologische Annahmen gezeigt. Darüber hinaus wurde die Dosisunsicherheit bei der Anwendung eines gemischten Strahlungsfeld-Partikel-Spektrums quantifiziert, wobei sich nicht vernachlässigbare, aber klinisch akzeptable Dosisunterschiede ergaben. Eine neuartige Methode die mehrere Ionenarten in einem Bestrahlungsfeld kombiniert um ein konstantes RBE generieren, welche RBE Unsicherheiten leichter Ionen reduzieren kann, wurde experimentell unter homogenen und heterogenen Bedingungen verifiziert. Die hier presentierten Untersuchugen tragen zur Reduzierung und Evaluation von Unsicherheiten in zukünftiger Teilcherapie bei.

Contents

Acronyms

^{4}He	helium ion
^{12}C	carbon ion
^{16}O	oxygen ion
^{20}Ne	neon ion
d	deuterium
p	proton
t	tritium
BP	Bragg-Peak
CICR	Combined Ion-Beam with Constant RBE
CNAO	National Centre for Oncological Hadrontherapy
CPU	Central Processing Unit
CSDA	Continuous Slowing Down Approximation
CT	Computer-Tomography
D_{RBE}	Biologically Weighted Dose
DCPT	Danish Centre for Particle Therapy
DDD	Depth-Dose Distribution
DG	Double Gaussian
DSB	Double Strand Break
DVH	Dose Volume Histogram
FLUKA	Fluktuierende Kaskade
FRoG	*Fast dose Recalculation on GPU*
FWHM	Full Width at Half Maximum
GPU	Graphics Processing Unit
GSI	Gesellschaft für Schwerionenforschung
H&N	Head and Neck
HIT	Heidelberg Ion-Beam Therapy Center
ICRU	International Commission on Radiation Units & Measurements
IMPT	Intensity Modulated Particle Therapy
LBNL	Lawrence Berkeley National Laboratory
LEM	Local Effect Model
LET	Linear Energy Transfer
LET_d	Dose-averaged Linear Energy Transfer

LQ	Linear Quadratic
MC	Monte Carlo
MIT	Multi-Ion Therapy
MKM	Microdosimetric Kinetic Model
mMKM	modified Microdosimetric Kinetic Model
MRFS	Mixed Radiation Field Spectra
OAR	Organ at Risk
PB	Pencil Beam
PRECISE	*PaRticle thErapy using single and Combined Ion optimization StratEgies*
QA	Quality Assurance
RBE	Relative Biological Effectiveness
RIFI	Ripple Filter
ROI	Region of Interest
RS	Range Shifter
SFUD	Single Field Uniform Dose
SIMT	Single Instruction Multiple Threads
SOBP	Spread-Out Bragg Peak
SPR_w^m	Stopping Power Ratio to Water
TCP	Tumor Control Probability
TG	Triple Gaussian
TPS	Treatment Planning System
WET	Water Equivalent Thickness

1. Introduction

1.1. Radiation Therapy

Although scientific attention is currently focusing on the raging 2020/2021 COVID-19 pandemic (128), cancer is still one of leading causes of death in the developed world. For 2020, the American Cancer Society projected $\sim$ 1.800.000 new incidents and $\sim$ 600.000 deaths caused by cancer in the United States America alone (126). Together with chemotherapy and surgery, radiation therapy is one of the most important treatment options of malignant tumours. Only months after the discovery of X-rays in 1885, the first patient was treated with X-rays (109; 34). Ionising radiation affects healthy tissue and tumour cells differently. Tumour cells have worse repair mechanics than healthy tissue, which can be exploited for treatment (118). Radiotherapy can be applied in multiple fractions that deliver the total prescribed ionising energy over the course of weeks. Due to the low costs compared to particle therapy and accessibility, radiation therapy with X-rays is currently the most common form of radiation therapy. However, the number of centres providing ionised particle therapy and patients that were treated with particle therapy is increasing in recent years (104).

The usage of proton (p) beams for cancer treatment has already been proposed in 1946 by Robert R. Wilson (148). Wilson argued that due to the finite and controllable range, as well as the favourable depth energy deposition, fast p allow for very conformal tumour irradiation. The amount of energy deposited by ions is inversely proportional to the penetration depth in a medium that peaks in the so-called Bragg-Peak (BP) after which the energy deposition drops to almost zero, sparing healthy tissue distally of the target. By overlapping multiple BPs of different ranges, i.e. energies with each other, a Spread-Out Bragg Peak (SOBP) can be formed that covers the entire tumour volume. In contrast, the energy deposition of X-rays decreases exponentially with depth delivering energy beyond the tumour. Schematic differences in energy deposition between a p SOBP irradiation and a X-ray treatment are displayed in figure 1.1. Except for a small region in the entrance, p radiation deposits less ionising energy to healthy tissue compared to X-rays for a similar target coverage.

The first clinical usage of light ions was pioneered at the Lawrence Berkeley National Laboratory (LBNL), California, which treated the first patient $\sim$ 8 years after Wilsons publication (114). At LBNL, light ions such as neon ion (^{20}Ne) or helium

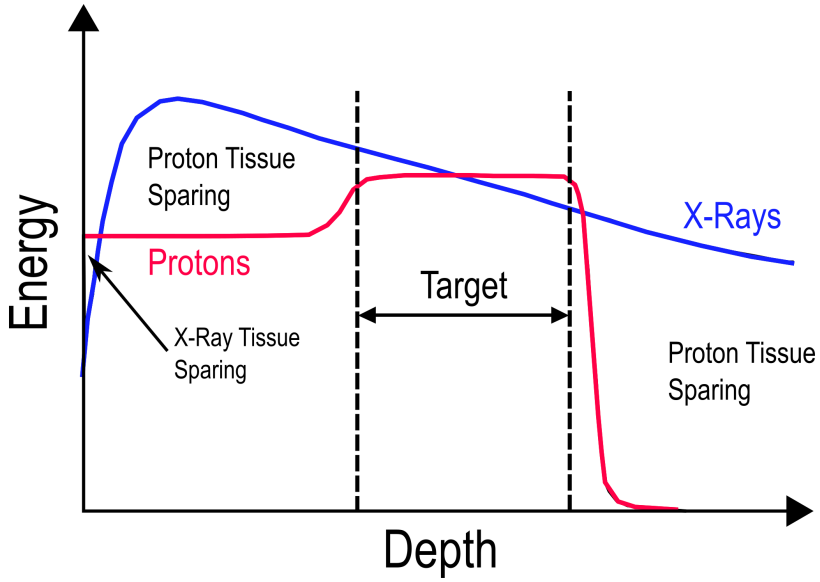

Figure 1.1.: The energy depositions of an X-ray beam and a p SOBP. For X-rays the in-depth energy deposition decreases exponentially after a short rise, while ions deposit their ionising energy inversely with depth. With particle therapy, ionising energy to tissue outside the target is reduced compared to X-rays. Figure adapted from Goitein (34).

ion (^{4}He) were investigated to treat cancer. Clinical trials at LBNL were eventually shut down in the last decade of the 20th century (114). In 2009, the Heidelberg Ion-Beam Therapy Center (HIT), Heidelberg, Germany started its patient treatment with actively delivered p and carbon ion (^{12}C) beams (21).
Particle therapy is individually tailored to every patient. Using a three-dimensional image of the patient, the energy as well as the position and intensity of every particle beam is adjusted to homogeneously irradiate the tumour. These *treatment plans* are created by dedicated Treatment Planning Systems (TPSs). Although all plans are checked for deliverability and dosimetric consistency usually before the first treatment (149), the exact energy distribution within the patient can still vary depending on the TPS prediction accuracy and uncertainties with the beam delivery or the patient. Deviations from TPS predictions are more likely in tissue-heterogeneous regions of the human body with analytical algorithms. Using an anthropomorphic head phantom, a recent study with p and ^{12}C ions showed that measurements deviated from TPS predictions around 4 % (91). Uncertainties can be nowadays taken into account during the treatment planning process with extra safety margins or robust optimisation (138). Even though the overall calculation accuracy is constantly improved, especially with the introduction of commercial Monte Carlo (MC) powered TPSs in p therapy (145), dose accuracy is still one the biggest concerns in particle therapy. Independent plan verification can potentially contribute to uncertainty reduction of intrinsic errors in the TPS predictions. To that end, independent

TPS verification at a p treatment facility was investigated in this work, potentially decreasing uncertainties within p therapy.
For the same deposited energy, the cell damage can vary between X-rays and fast charged particles. Therefore, particle therapy uses the concept of Relative Biological Effectiveness (RBE) to relate clinical experience obtained with X-rays to ions. The exact determination and application of variable RBE is still highly discussed (99). For clinical usage of p, an RBE of 1.1 is clinically used worldwide, even though multiple studies showed varying RBE with Linear Energy Transfer (LET) (99). For other light ions, such as ^{4}He or ^{12}C, RBE values in the range from ~ 2 to ~ 5 were observed *in-vitro* and *in-vivo* experiments (58; 113; 89). The uncertainty in RBE prediction is reflected by the variety phenomenological and mechanistic dose models to predict RBE of p and other light ions (41; 28; 46; 144; 86; 76). These models usually use both physical and biological variables such as LET or X-ray cell sensitivity as principal inputs. However, the exact biological variables are *a priori* mostly unknown in patients and can only be estimated from previous treatment experience of similar tumour histology (139). Therefore, particle therapy is accompanied by an intrinsic uncertainty stemming from RBE prediction accuracy. By investigating the biological sensitivity of treatment plans with ions prior to delivery, i.e. quantifying RBE uncertainties, the latter could be revealed and potentially reduced with new treatment planning.

1.2. Thesis Outline

This work is presented as a cumulative thesis that shows the development and verification of novel methods that evaluate, reduce, and overcome intrinsic uncertainties of modern particle therapy, e.g. plan conformality, dose prediction accuracy, and RBE variations of light ions. An introduction to the physics of charged particles with for particle therapy relevant kinetic energies is given in chapter 2. Important methods, concepts, and techniques for this work are introduced in chapter 3. Afterwards three publications are put forward in chapter 4 that

4.A) establish and verify a fast secondary dose calculation engine at a proton therapy centre to independently verify treatment plans and provide additional clinically relevant information such as p RBE

4.B) investigate a method for fast biological dose calculation for actively scanned ^{4}He beam therapy and determine the sensitivity of a biophysical dose model to clinical parameters

4.C) develop, verify, and analyse a method for multi-ion particle therapy that delivers a constant physical dose and constant RBE to the target.

The results and implications of the findings of these publications are discussed and summarised in chapters 5 and 6, respectively.

2. Physical Rationale of Charged Particles

2.1. Energy Loss

The stopping power S, i.e. the energy loss per unit length ($-\,\mathrm{d}E/\,\mathrm{d}x$) of an charged particle (ion) in matter can be described by three components,

$$S = -\frac{\mathrm{d}E}{\mathrm{d}x} = \overbrace{S_{el} + S_{nuc}}^{\text{col}} + S_{rad}, \tag{2.1}$$

where the collision (col) stopping power is the sum of inelastic interactions with electrons (S_{el}) and elastic interactions with the nucleus (S_{nuc}) (49). The radiative energy loss (S_{rad}) scales inversely with the square root of the projectile mass and can therefore be neglected in particle therapy due to the high particle masses (49). For high particle energies, S_{nuc} is also negligible while at very low energies for high Z particles such as ^{12}C or oxygen ion (^{16}O), S_{nuc} dominates over the electric stopping power. S_{el} and S_{nuc} for p and ^{12}C ions as a function of particle energy are shown in figure 2.1. Not accounting for S_{nuc} and S_{rad}, the mean energy loss per unit length ($-<\mathrm{d}E/\,\mathrm{d}x>$) can be described with the Bethe-Bloch formula

$$-\left\langle\frac{\mathrm{d}E}{\mathrm{d}x}\right\rangle \approx < S_{el} > = \frac{\rho 4\pi N_A r_e^2 m_e c^2 Z_p^2 Z_t}{A_t \beta^2}\left[\frac{1}{2}\ln\frac{2m_e c^2\beta^2 W_{max}}{I^2(1-\beta^2)} - \beta^2 - \frac{\gamma}{2} + SBB\right], \tag{2.2}$$

where ρ is the mass density, N_A is the Avogadro constant, Z_p and Z_t are the projectile and target charge, respectively (52). A_t is the targets atomic mass, while the mass and radius of an electron are m_e and r_e, respectively. W_{max} is the maximum energy that can be transferred to an electron in a single event, while the mean excitation energy for an electron is I. For water in liquid form, the International Commission on Radiation Units & Measurements (ICRU) recommends an I value of 78 eV, with an uncertainty (standard deviation) of 2 eV (51; 52). The original Bethe-Bloch formula did not account for extremely high (relativistic) and low particle energies. To that end, energy loss corrections for shell (SBB) (at low particle energies where the velocity of bound atomic electrons can not be neglected (49)) and density (γ) are added in equation 2.2. Lastly, β is the relative velocity of the projectile with respect to the speed of light c. In a first approximation the energy-loss of ions in matter is inversely proportional to β^2.

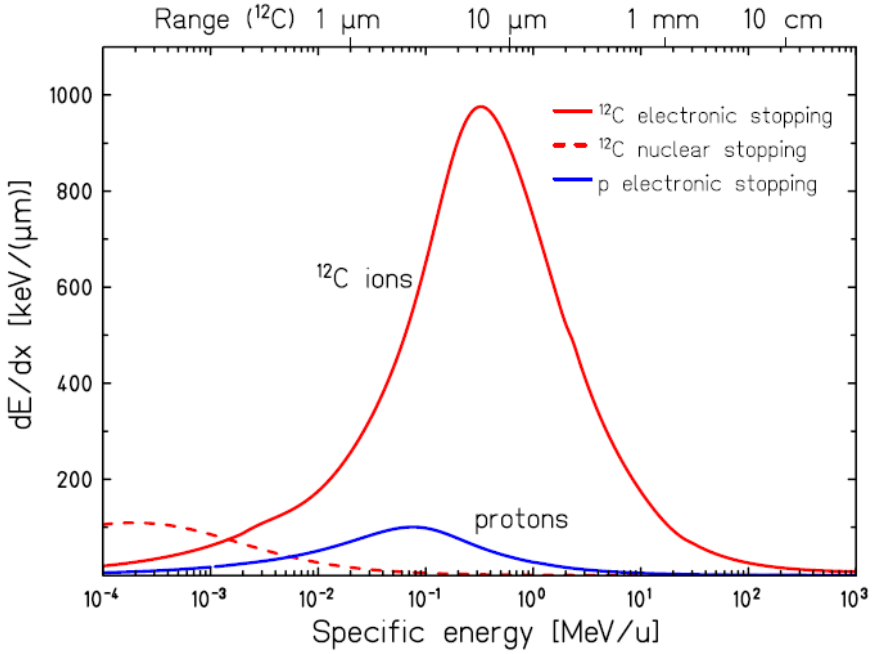

Figure 2.1.: Energy loss of p and ^{12}C in water is depicted as a function of particle energy. For ^{12}C, the remaining range is drawn on the top axis. Taken from Schardt et al. (114).

At low particle energies, ions recombine with free electrons in the material and the effective charge of an ion beam (Z_{eff}) reduces. Z_{eff} can then be described by

$$Z_{\text{eff}} = Z_p[1 - exp(-125\,\beta\,Z_p^{-2/3})], \tag{2.3}$$

where Z_p is again the charge of the projectile (114). The combination of increasing energy loss at low particle particle velocities ($\mathrm{d}E/\,\mathrm{d}x \propto 1/\beta^2$) and decreasing Z_{eff} results in the so-called BP, i.e. a short rise of energy deposition, followed by a quick descend. The depth energy deposition curves of a p and ^{12}C BP are displayed in figure 2.2. A BP can be separated in multiple regions; the plateau is the most proximal part of a BP and is followed by the peak itself. The proximal and distal edge of a BP refer to the energy deposition rise and fall-off before and after the peak, respectively. For ions other than p, there is a tail after the peak due to particle fragmentation (c.f. section 2.2).

An important quantity for radiation biology is the LET of ions. The ICRU defines LET [keV/μm] as the amount of energy loss per unit length that is lost by an ion due to inelastic electronic collisions (in a volume), subtracting the amount of energy that is transferred out (of the volume) by secondary electrons with energies larger than a threshold Δ (50). The restricted LET is defined as

$$\text{LET}_\Delta = \frac{\mathrm{d}E_\Delta}{\mathrm{d}x}. \tag{2.4}$$

For an infinite high threshold of Δ, LET_Δ is equivalent to S_{el}. Numerous studies have investigated the influence of LET on the RBE (c.f. section 3.3.2) for p (147;

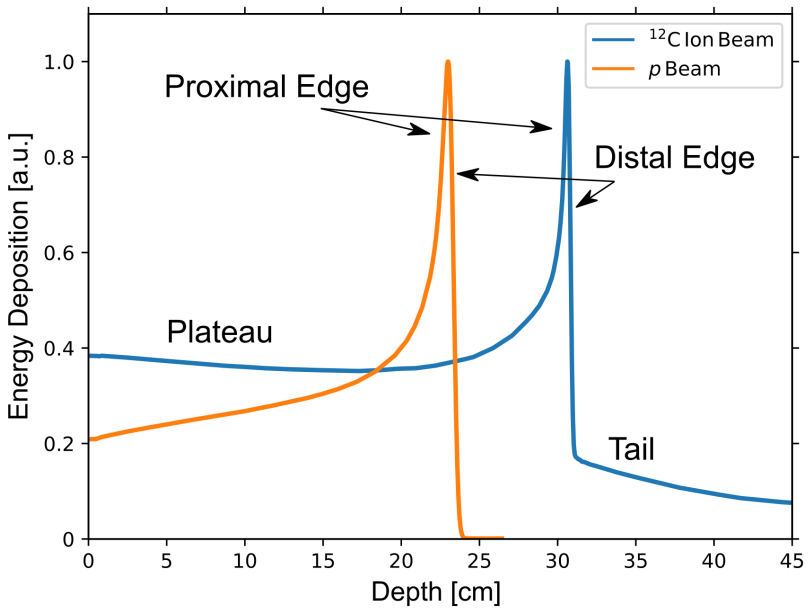

Figure 2.2.: Overview of p and ^{12}C BP in-depth energy-deposition profiles in water. The different sections of the BPs are labelled.

144; 86; 76). To quantify the LET of a mixed particle radiation field, i.e. different ion species and particle energies in a volume, the LET is either averaged over the track length of the particles or by their dose deposition (c.f. section 3.2). The latter approach is more often used and the (unrestricted) Dose-averaged Linear Energy Transfer ($\mathrm{LET_d}$) can be defined as

$$\mathrm{LET_d} = \frac{\int \Phi \, S_{el}(E) \, S(E) \, \mathrm{d}E}{\int \Phi \, S(E) \, \mathrm{d}E}, \tag{2.5}$$

where Φ is the particle fluence and $S(E)$ the energy dependent stopping power (7). Note that for e.g. biological modelling, sometimes only $\mathrm{LET_d}$ of individual ion species, e.g. of $\mathrm{Z} = 1$ (p, deuterium (d), and tritium (t)), particles are included in equation 2.5.

2.2. Nuclear Fragmentation

While traversing through matter, ions can interact with the target nuclei via the strong nucleon-nucleon force either elastically or inelastically (34). An ion that elastically interacts with a target nuclei is heavily scattered and loses a considerable amount of its kinetic energy (34). The projectile and target stay thereby intact. The inelastic collision between a projectile and a target nucleus can be described by the *abrasion-ablation* model in a two step process (124; 114). In the first step, the

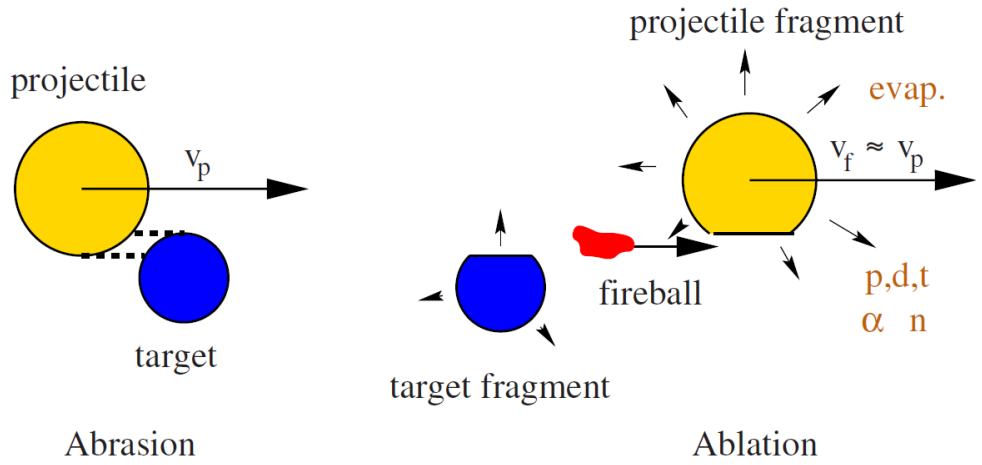

Figure 2.3.: Visualisation of the *abrasion-ablation* model. A detailed description is given in the main text (c.f. section 2.2). Figure taken from Schardt et al. (114).

overlapping regions of the projectile and the target nucleus merge in the so-called *fireball*. A partial overlap of target and projectile is thereby more likely than a full overlap. In the second step, secondary particles, i.e. *fragments*, with approximately the same velocity and beam direction of the projectile emerge from the fireball. A schematic of the two processes of the *abrasion-ablation* model is visualised in figure 2.3. Fragments with lower mass/charge are more likely and traverse further than a primary ion, creating an energy deposition tail after the BP. Furthermore, they also scatter more than the primary ions and therefore influence the overall lateral beam shape. For light ions with $Z > 1$, secondary fragments considerably contribute to the overall dose of a pencil beam. Figure 2.4 (left) displays the number of secondary per primary particles (N/N_0) as a function of penetration depth for a 400 MeV/u ^{12}C ion beam in water. With increasing penetration depth, the number of Hydrogen (H), Helium (He), Lithium (Li), Beryllium (Be) and Boron (B) ions, i.e. secondaries, outweighs the number of primary ^{12}C ions. The BP position is indicated by a vertical black dashed line. The relative contribution of primary, secondary, and tertiary (i.e. fragments produced by secondary particles) fragments to the total deposited energy of a 670 MeV/u ^{20}Ne beam are shown in the right panel.

Inelastic interactions with the target nuclei reduce the number of primary projectiles with range. For high particle energies, the fluence after a penetration depth ($\Phi(d)$) can be described by an exponential function

$$\Phi(d_m) = \Phi_0 \, e^{-\frac{d_m}{\lambda_m}}, \tag{2.6}$$

where Φ_0 is the initial particle fluence, d_m is the distance in matter, and λ_m is a material and particle specific absorption length (52). For ^{12}C ions, 50 % of ^{12}C ions remain at $d_m = 18$ cm in water, assuming a λ_m of 25.9 cm (52).

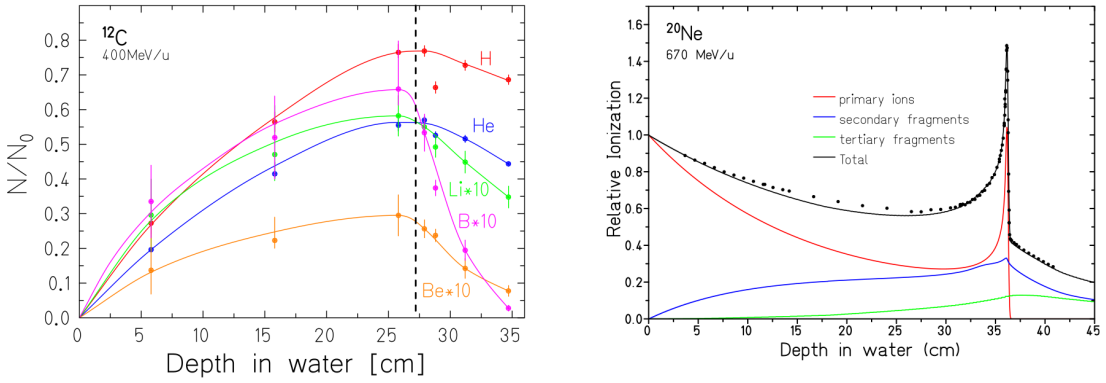

Figure 2.4.: In the left panel, the buildup of secondary ions (H, He, B, Li, Be) in water for a 400 MeV/u ^{12}C ion beam is shown. The BP is indicated by the vertical black dashed line. In the right panel, the energy deposition of primary, secondary, and tertiary fragments are visualised for a 670 MeV/u beam. Figures adapted from Schardt et al. (114).

2.3. Range

The range of a particle beam is the length it traversed through a medium. Using the Continuous Slowing Down Approximation (CSDA) the range (R) can be calculated as a function of energy (E) (114; 52)

$$R(E) = \int_E^0 \left(\frac{\mathrm{d}E'}{\mathrm{d}x}\right)^{-1} \mathrm{d}E'. \tag{2.7}$$

The range of a particle beam is direct proportional to its atomic number (A) over the square of its charge (Z) (52),

$$R \propto A/Z^2. \tag{2.8}$$

Figure 2.5 shows the ranges of p, ^{4}He, ^{12}C, ^{16}O, and ^{20}Ne beams in water. A non-linear dependency of range to the initial particle energy can be seen. For the same beam energy, ^{20}Ne ions have the smallest range of the investigated particles. p and ^{4}He beams have approximately the same range in water for the same energy, due to the A/Z^2 dependency. The CSDA range does not necessarily equal the penetration depth in a medium as the particle also undergoes lateral scattering. As heavier ions such as ^{12}C or ^{16}O undergo little lateral scattering (c.f. section 2.5), the CSDA range is a good first order approximation (118; 67).
In radiation therapy, the range of a beam is often described by the point where the beam energy deposition falls to 80% of its maximum (R_{80}). For p beams, R_{80} also nearly corresponds to the point where 50% of the initial protons are absorbed (34). The concept of range can also be extended to include biological scaling factors e.g. RBE (c.f. section 3.3.2) (15).

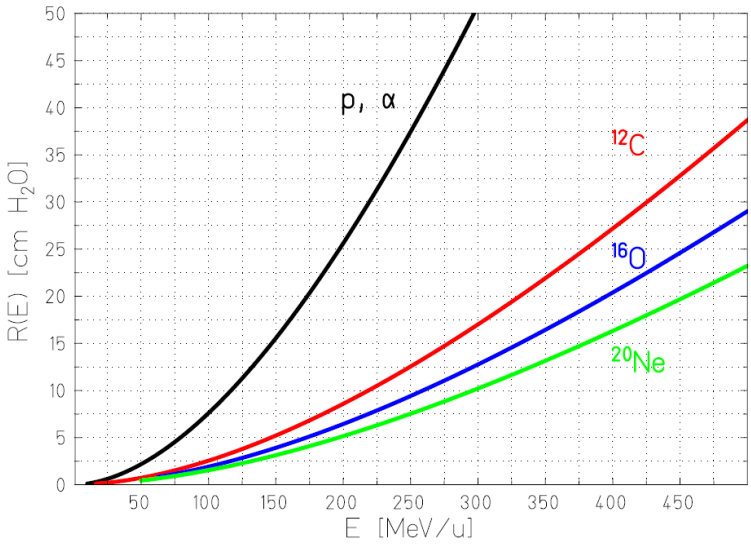

Figure 2.5.: Beam range R of different ions in water as a function of kinetic energy. α refers to ^{4}He ions. Taken from Schardt et al. (114).

2.4. Range Straggling

The energy loss of a particle is a stochastic event. Two particles with the same initial kinetic energy and traversing the same medium might not have the same range. These differences in range are called *range straggling*, yielding a broadened BP (114). For thin absorbers, i.e. a small number of interactions, the stochastic energy loss can be described by the Vavilov distribution (140; 114), while for a large number of interactions (or thick absorbers) the energy loss follows a Gaussian distribution (12; 2). The ratio of the BP broadening width (σ_r) to the average beam range (R) is almost constant and can be described by

$$\frac{\sigma_r}{R} = \frac{1}{\sqrt{M}} f\left(\frac{E}{Mc^2}\right), \tag{2.9}$$

where E is the initial beam energy, M is the projectile mass, c is the speed of light and f is a material dependent function (110; 114). As σ_r/R is indirect proportional to the square root of the particle mass M, light ions such as ^{4}He or ^{12}C feature smaller BP widths than p. To that end, a Ripple Filter (RIFI) (143) can be employed that artificially widens the BP, reducing the number of beam energies to create a SOBP.

2.5. Lateral Scattering

Particle beams traversing matter exhibit a beam widening with penetration depth that is caused by elastic Coulomb interactions of the ions with the target nuclei.

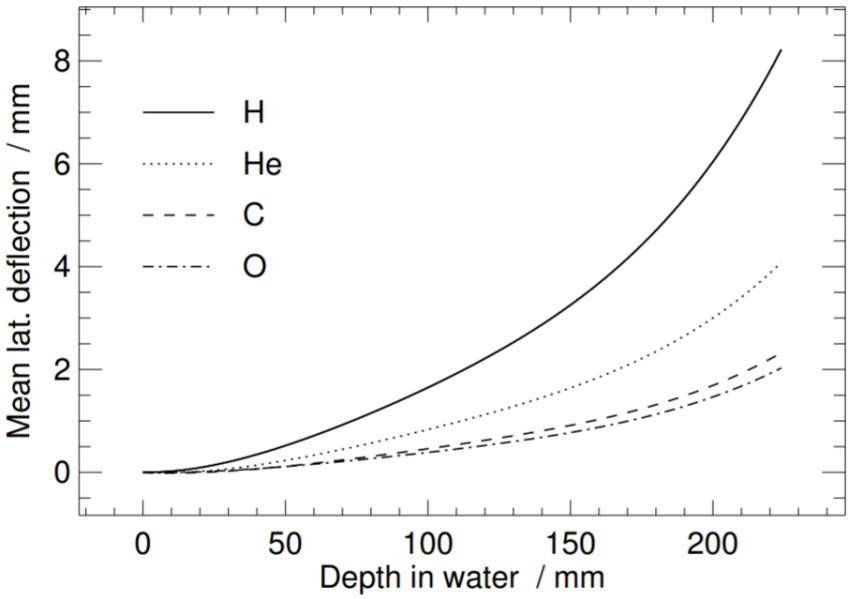

Figure 2.6.: Comparisons of lateral spread of p, ^{4}He, ^{12}C, and ^{16}O ion beams in water. Figure taken from Parodi (101).

Individual elastic Coulomb interactions of the projectile with the target nuclei often result in only a small deflection from the primary particle path. However, particles undergo a large number of Coulomb interactions with the nuclei and the combination of several deflections is called *multiple-Coulomb scattering* (MCS) (114; 52). MCS is the main source of beam widening and the lateral scattering from inelastic collisions with target electrons can be neglected in particle therapy (114).
The scattering by Coulomb interactions for ions in matter was explored theoretically by Molière using the the Thomas-Fermi method (95; 96). In a first approximation, the deflection angle σ_Φ of a particle beam traversing through a length d in matter with the radiation length L_{rad} can be described with the so-called *Highland approximation* by a single Gaussian distribution with zero mean and standard deviation given by

$$\sigma_\Phi[\text{rad}] = \frac{14.1\,\text{MeV}}{\beta pc} Z_p \sqrt{\frac{d}{L_{\text{rad}}}} \left[1 + \frac{1}{9}\log_{10}\left(\frac{d}{L_{\text{rad}}}\right)\right], \tag{2.10}$$

where β is the relative particle velocity to the speed of light (c), Z_p is the particle charge and p the beam momentum (114; 43). Note that equation 2.10 is only valid when $d \ll$ remaining ion range, i.e. for thin absorbers (35). The deflection angle is dominated by the $1/\beta p$ term of equation 2.10, resulting in lower deflection angles for higher Z particles (118). A comparison of the mean lateral deflections of different ion beams is shown in figure 2.6. Light ions such as ^{16}O, ^{12}C, or ^{4}He scatter considerably less than p, making them especially suited for therapy critical structures are located lateral to the target.

3. Material and Methods

3.1. Beam Delivery

3.1.1. Particle Accelerators

In particle therapy, particle accelerators are used to bring ions to their therapeutic kinetic energy. The limiting factor for all particle accelerator types is that for clinical practice, they should be able to produce ion beams with ranges of $\sim 30\,\mathrm{cm}$, to reach any tumour location within the human body (114). Currently, the two main types of accelerators employed for particle therapy are cyclotrons, and synchrotrons, while linear accelerators are mostly used as pre-accelerators for synchrotrons.
Cyclotrons accelerate ions by combining an alternating electric field that is perpendicular on a constant magnetic field. Due to the Lorentz-force, the particles are bound to a spiral path and exit the cyclotron with a fixed energy that is quadratically dependent on the magnetic field strength B and size (radius R) of the cyclotron. For non-relativistic particles, the energy of an ion E_{exit} with charge Z and mass M after leaving the cyclotron is

$$E_{exit} = \frac{(ZeRB)^2}{Au}, \tag{3.1}$$

where e is the electric charge and u the atomic mass (24). At relativistic particle energies, the frequency of the alternating electric field or the magnetic field strength has to be adjusted to account for the increasing particle mass. E_{exit} defines the maximum energy, i.e. maximum range of the therapeutic beam. For lower beam ranges, degraders of varying thickness are inserted upstream of the patient that reduce E_{exit} (114). Due to nuclear interactions, these degraders produce secondary protons and reduce the overall beam intensity. Furthermore, in theory, the degraders also introduces additional range straggling that flattens the energy deposition peak and therefore reduces the peak-to-plateau ratio, which in reality can be reduced with a beam energy cleaning process (117; 114). Nevertheless, cyclotrons offer increased particle-rates compared to synchrotron accelerators (118) as the particles are extracted as an (almost) continuous particle flux. In particle therapy, cyclotrons are only used to accelerate p, despite recent efforts to develop a $Z > 1$ light ion cyclotron (56).
In a synchrotron, the particle beams are accelerated by HF-modules after being

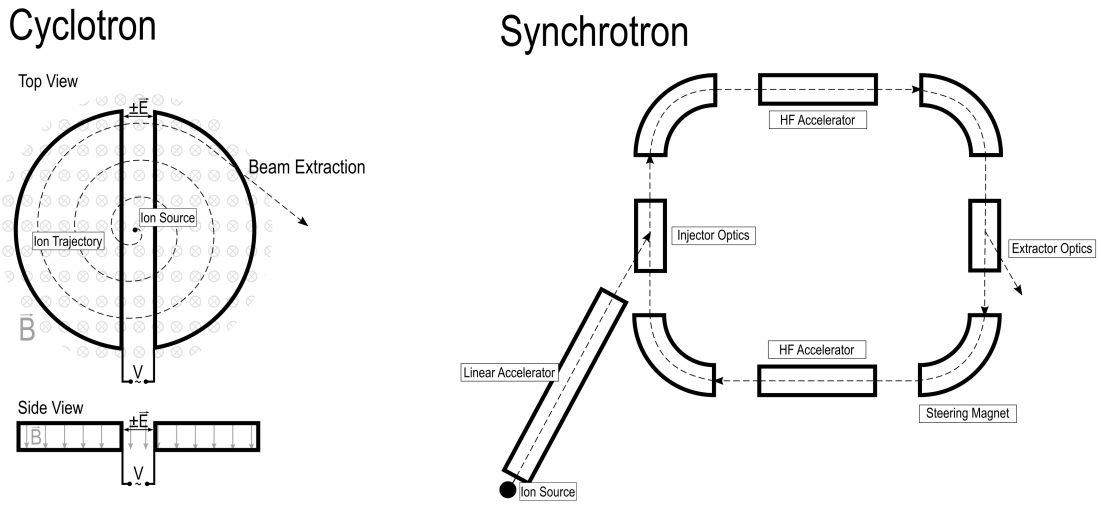

Figure 3.1.: Schematics of cyclotron and synchrotron accelerators are shown. For the cyclotron accelerator, the electric ($\vec{E}$) and magnetic field ($\vec{B}$) are displayed. Invididual components of the synchrotron are labelled. Figure inspired from Demtröder (24).

injected by a linear accelerator. The particle trajectory is determined by steering magnets, that with increasing particle energy have to be adjusted in their field strength. Depending on the ion source and steering magnet strength synchrotrons can accelerate any particle, making them specially suited for ion therapy with high Z particles. Compared to cyclotrons, which produce a steady stream of particles, synchrotrons accelerate ions in individual spills. As spills are accelerated and extracted one at a time, there is usually a pause in the order of a few seconds between two consecutive spills (52). However, novel techniques are currently investigated that potentially decrease spill pauses and thereby could increase the beam intensity (122).
Schematics of cyclotron and synchrotron (that is combined with a linear injector) accelerators are displayed in figure 3.1. The beam trajectory is visualised. For the cyclotron, the magnetic and electric field directions are displayed.

3.1.2. Active Beam Delivery

Passive beam delivery uses scatterers or wobbling magnets to widen a finite beam in combination with collimators as compensators to shape the ion field to the tumour (20). These compensators and collimators had to be specifically tailored for every patient and tumour.
Active beam delivery has been independently developed by the *Paul Scherrer Institut* (Villingen, Switzerland) and the Gesellschaft für Schwerionenforschung (GSI) (Darmstadt, Germany) (106; 38). Compared to passive beam delivery, active beam

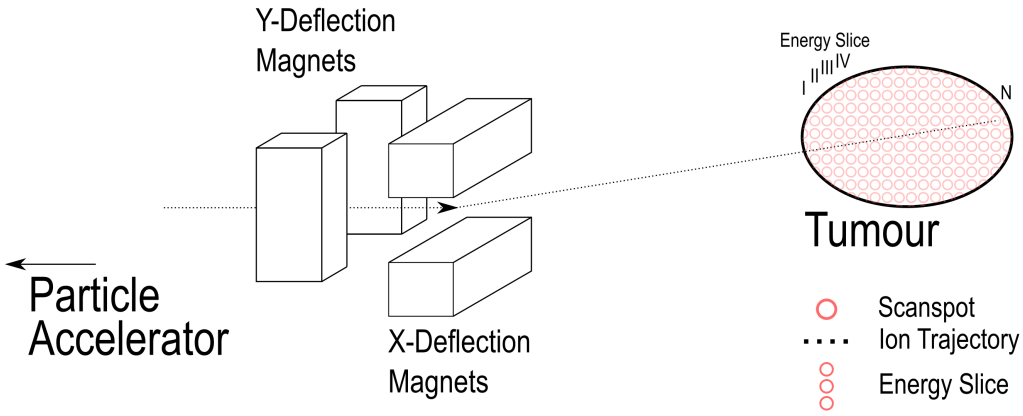

Figure 3.2.: The main features of active beam scanning are shown. Beams are deflected by two scanning magnets. By varying the beam energy or degrader insertion, different beam depths in the patient are reached.

scanning requires no material (other than degraders with cyclotrons accelerators) upstream the patient to irradiate the tumour. Ion beams are deflected with so-called *scanning magnets* by varying their magnetic field strength, exploiting the Lorentz-force on charged particles (visualised in figure 3.2). The beam depth in the patient is set by variation of the beam energy or insertion of degraders for synchrotron or cyclotron facilities, respectively. To irradiate a tumour, multiple spots in the tumour are targeted that together homogeneously irradiate the volume. A single spot with a certain energy is called a Pencil Beam (PB). Compared to passive beam delivery, active beam scanning effectively spares healthy tissue (114). Dependent on the tumour location, the choice of the beam delivery vector can influence the energy deposition to normal tissue and other Region of Interests (ROIs). To that end, most facilities nowadays employ gantries that rotate the beam line and particle beam exit around the patient.

3.1.3. Heidelberg Ion-Beam Therapy Center

HIT is a spin-off company from the ^{12}C treatment facility at the GSI (39). Since facility startup in 2009, the HIT has been treating > 5000 patients with p and ^{12}C ions (87). The most common cancer indications at HIT that are treated with ions are Head and Neck (H&N) tumours (1). Furthermore, ^{4}He and ^{16}O ions are available for biological and physics research (132; 131; 80). HIT is one of only two centres in the world with a light ion ($Z \geq 6$) gantry for patient treatment, the other one being in Japan (39; 54). The beam gantry adds additional degrees of freedom in the beam delivery for light ion beam therapy that are otherwise unobtainable, resulting in potentially improved normal tissue sparing.
At HIT, there are three treatment rooms (1x gantry and 2x horizontal) and one experimental room (horizontal). Figure 3.3 shows an overview of the HIT facility.

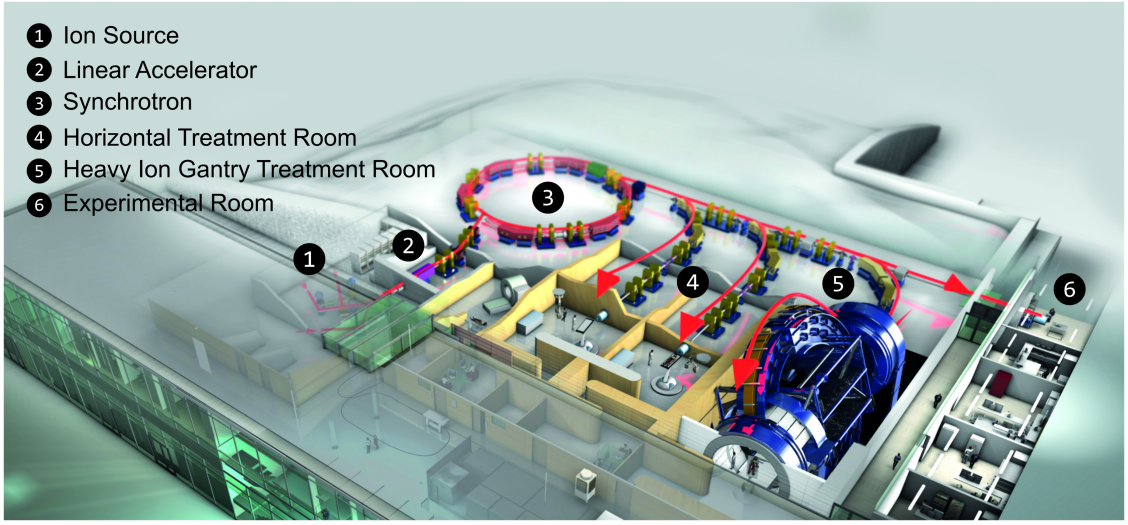

Figure 3.3.: The HIT layout with beam delivery components and treatment rooms. The red arrow shows the beam trajectory from the source to the individual treatment rooms. Figure adapted from HIT stock images, courtesy of HIT.

The ions are generated by a source, pass a linear accelerator before entering the 20 m (diameter) synchrotron (39). In the synchrotron, ions are accelerated up to 430 MeV/u, yielding particle depths of ~ 30 cm in water. For treatment, 255 energies with up to 1.5 mm range difference between them are commissioned (102). Through a dedicated and near vacuum beam-line, the synchrotron delivers the ions to the treatment and experimental rooms.

3.2. Dose

Dose (D [Gy]) is one of the most important quantities in radiation therapy. D is defined as the absorbed energy from radiation E_{rad} per mass m (49)

$$D[\text{Gy}] = \frac{E_{\text{rad}}}{m}. \tag{3.2}$$

In SI units, Gy is equivalent to J/kg and is in particle therapy often scaled for its biological efficiency (cf. equation 3.15). D in a thin absorber can also be expressed with the particle fluence $\Phi[\text{cm}^{-2}]$, their respective energy loss in keV/μm and the mass density of the material (ρ [g/cm^3]) (114)

$$D\,[\text{Gy}] = \Phi \cdot 1.6 \cdot 10^{-9} \cdot \frac{dE}{dx} \cdot \frac{1}{\rho}. \tag{3.3}$$

A similar microscopic quantity to D is the specific energy (z), which is defined as the imparted energy by ions (ϵ) in a mass (m) (49),

$$z = \frac{\epsilon}{m}. \tag{3.4}$$

3.3. Biological Dose

3.3.1. Radiation Damage

The DNA is the most sensitive part of a cell. Ions can damage cells directly with hits to the DNA or indirectly by production of free radicals that then damage the DNA (114). Compared to low LET radiation, the damage from direct hits to the cell is increased for light ions with high LET (53; 114). However, indirect damage due to free radicals causes the largest amount of cell lesions (114). The most significant kinds of radiation damage to the DNA are: I) single strand breaks that are the most readily repairable kind of damage, while II) a Double Strand Break (DSB) is considerably more lethal as DNA repair is complicated (66). If multiple single strand breaks and/or DSBs are within a small region, it is considered complex cell damage (118). Complex cell damage can trigger multiple repair mechanisms in the cell at once, which, when interfering with each other, reduce the chance for a successful repair, lowering the cell's overall survival probability (116). The track structure of the ionising particle has a significant impact on the survival probability of a cell, as a very localised energy deposition leads to a higher probability of complex cell damage (114). Figure 3.4 shows the dose-track structure of photons (X-rays) and ^{12}C ions between 1 MeV/u and 200 MeV/u for constant dose. While X-rays have a bath of low dose over the investigated area, the energy deposition of ^{12}C ions largely depends on the beam energy. ^{12}C ions at very low energies (1 MeV/u, corresponding to $\sim 10\,\mu$m of range, c.f. figure 2.1), deposit their energy in localised position with no dose elsewhere. Contrarily, high energy ^{12}C ions (200 MeV/u) show both, a bath of low dose contribution combined with a shower of high dose in small areas. For a single ion, the lateral energy deposition track structure can for example be described by the *Kiefer–Chatterjee* model that combines a constant core with a radial decreasing energy deposition. Thereby, the core and radial component are not continuous (16; 60).

Under the theory of dual radiation action (TDRA) (59), the mean yield of lesions ($Y(D)$), i.e. mean damage to a cell, as function of dose (D) can be described with a linear α and quadratic β term (4) by

$$Y(D) = \alpha D + \beta D^2. \tag{3.5}$$

As the combination of sub-lesions from multiple doses yield more overall lesions (e.g. two sub-lesions combining to one lesions), the expected number of lesions $Y(D_1, D_2)$ of two doses D_1 and D_2 is bigger than the sum of respective individual lesions. For two doses the expected yield of lesions can be calculated by

$$Y(D_1, D_2) = \overbrace{\alpha_1 D_1 + \alpha_2 D_2}^{\text{I}} + \underbrace{\beta_1 D_1^2 + \beta_2 D^2 + 2\sqrt{\beta_1 \beta_2} D_1 D_2}_{\text{II}}, \tag{3.6}$$

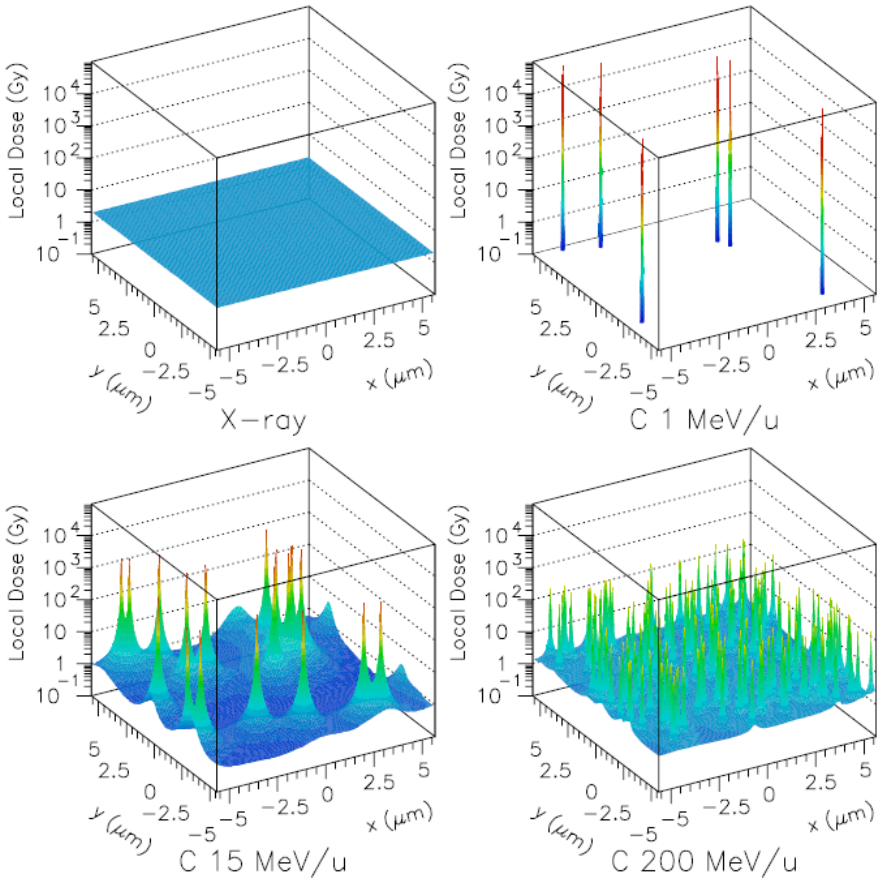

Figure 3.4.: Dose-track structure for photons and ^{12}C ions of three different energies. The delivered dose in all panels is constant. Taken from Scholz et al. (121).

where α_1/β_1 and α_2/β_2 are the linear/quadratic terms of D_1 and D_2, respectively (4). By sub-dividing D_1 and D_2 further and combining the individual linear terms (I) and quadratic terms (II), it is clear that the yield of lesions for N sub-doses can be generalised with

$$Y(D_1, D_2) = \overbrace{\sum_{i=1}^{N} \alpha_i D_i}^{\text{I}} + \underbrace{\Big(\sum_{i=1}^{N} \sqrt{\beta_i} D_i\Big)^2}_{\text{II}}. \tag{3.7}$$

The mean survival of cells after irradiation can then be described with the Linear Quadratic (LQ) model (31). In the LQ model, the cell survival as function of dose ($S(D)$) is described by

$$S(D) = \exp(-\alpha D - \beta D^2), \tag{3.8}$$

where D is dose, α and β are the dose-averaged linear ($\overline{\alpha}$) and quadratic ($\overline{\beta}$) dependency term, respectively. $\overline{\alpha}$ and $\overline{\beta}$ can be calculated with

$$\begin{aligned} \overline{\alpha} &= \frac{\sum_{i=0}^{N} \alpha_i D_i}{\sum_{i=0}^{N} D_i}, \\ \overline{\beta} &= \left(\frac{\sum_{i=0}^{N} \sqrt{\beta_i} D_i}{\sum_{i=0}^{N} D_i}\right)^2. \end{aligned} \tag{3.9}$$

3.3.2. Relative Biological Effectiveness

For the same D, the cell survival can vary with the cell type, radiation quality (8) and other factors such as medication (drugs) (5; 70) or oxygenation level (32). To that end, the RBE of radiation is defined as the quotient of a reference dose (D_r) and a comparing dose (D_c) that yields the same cell survival

$$\text{RBE} = \left.\frac{D_r}{D_c}\right|_{\text{Survival}}. \tag{3.10}$$

In particle therapy, due to $\sim$ 100 year of clinical experience with X-rays, D_r is usually from low LET photons, and D_c refers to ions. Despite various studies that revealed an RBE dependency with LET_d, RBE of p is assumed to be 1.1 in clinical practice world-wide (100; 99), while for light ion therapy, there are different mechanistic and phenomenological models to describe the biological effect. A comparison of the most used mechanistic RBE models is given elsewhere (129). From the LQ model (equation 3.8) and equation 3.10, the RBE as a function of D_c and LQ parameters α_c, β_c and α_r, β_r for reference and comparing cell survival, respectively, can be determined as

$$\text{RBE} = \frac{1}{D_c}\sqrt{\frac{\alpha_c D_c + \beta_c D_c^2}{\beta_r} + \Big(\frac{\alpha_r}{2\beta_r}\Big)^2} - \frac{\alpha_r}{2 D_c \beta_r}. \tag{3.11}$$

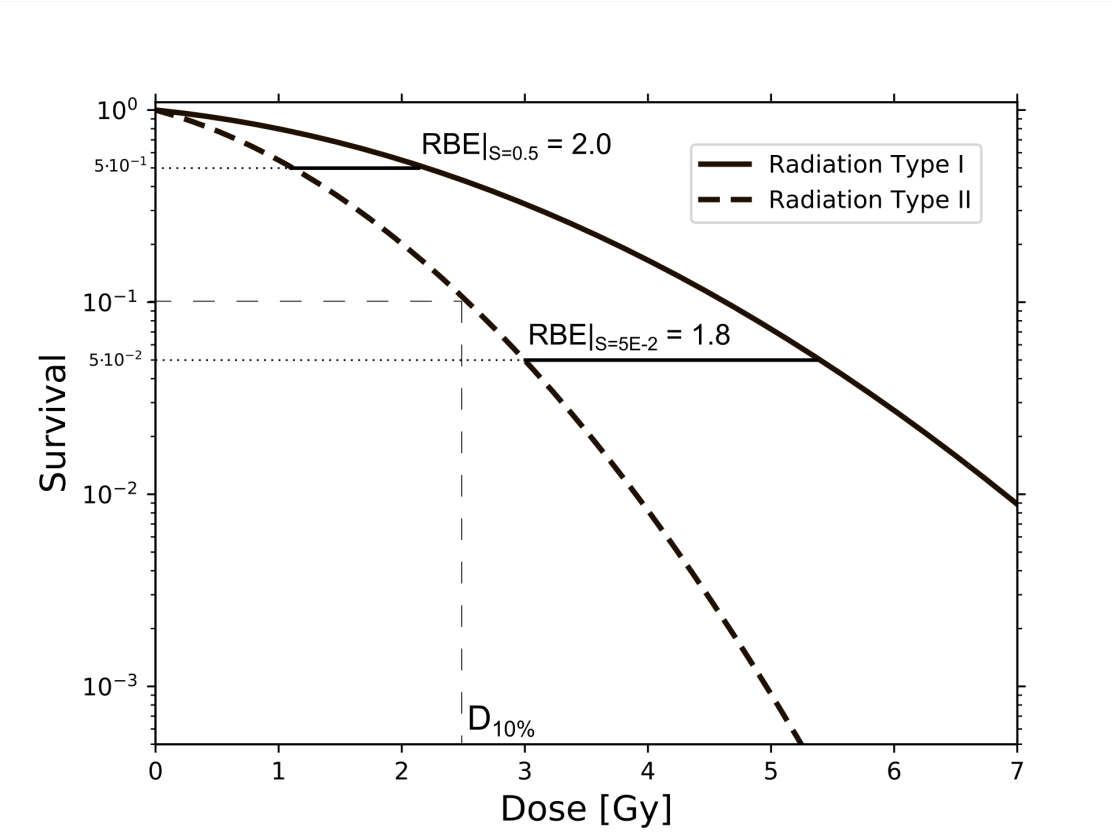

Figure 3.5.: Cell survival curve of two radiation types. The concept of RBE at different survival levels and D_{10} is visualised.

Figure 3.5 shows the schematic cell survival curves of two radiation types and therein a visualisation of RBE. Moreover, the exemplary concept of D_{10}, that corresponds to D that yields 10% cell survival is shown. As can be seen from equation 3.11, the RBE varies with the survival level $(-\ln(S_c) = \alpha_c D_c + \beta_c D_c^2)$.
To estimate RBE as a function of D_c and reference LQ parameters, the quotient of the linear and quadratic LQ parameters of reference and comparison S curves is introduced. The linear component is defined as

$$\mathrm{RBE}_\alpha = \frac{\alpha_c}{\alpha_r}, \tag{3.12}$$

while the ratio of the quadratic LQ terms models the survival difference of reference and comparing for high doses and is defined as

$$\mathrm{RBE}_\beta = \frac{\beta_c}{\beta_r}. \tag{3.13}$$

Inserting the linear (RBE_α) and quadratic (RBE_β) ratio terms in equation 3.11, one obtains

$$\mathrm{RBE} = \frac{1}{D_c}\sqrt{\frac{\alpha_r\,\mathrm{RBE}_\alpha\,D_c + \beta_r\,\mathrm{RBE}_\beta\,D_c^2}{\beta_r} + \left(\frac{\alpha_r}{2\beta_r}\right)^2} - \frac{\alpha_r}{2D_c\beta_r}. \tag{3.14}$$

As can be seen, RBE is only dependent on (α_r/β_r) and the scaling factors RBE_α and RBE_β, as well as D_c. The Biologically Weighted Dose ($\mathrm{D_{RBE}}$) is obtained by multiplying physical dose (D) with RBE

$$D_{\mathrm{RBE}} = \mathrm{RBE} \cdot D. \tag{3.15}$$

3.3.3. Local Effect Model

The Local Effect Model (LEM) version I is the clinically applied biophysical dose model for ^{12}C ion therapy at HIT (21) and was previously also employed for ^{12}C ion therapy at GSI (123). The principal idea of LEM version I is that dose induced damage in a small sub-volume of a cell is independent of the radiation quality that delivered it. Biological studies showed that LEM version I overestimated the RBE in the entrance channel, i.e. at low LET, and underestimates RBE in the target (58; 27; 90). In the latest LEM version (IV), the production of single strand brakes and DSBs in the cell are determined for light ions and then correlated to X-ray radiation to estimate RBE, improving the cell survival predictions (29). At high doses, the cell survival curve flattens (3). The reduced RBE is taken into account in the LEM by introduction of a dose threshold (D_t), after which a linear model is used to calculate $\mathrm{D_{RBE}}$. For an ion beam of dose D and linear quadratic parameters α_{ion} and β_{ion}, $\mathrm{D_{RBE}}$ can be calculated by

$$-\ln(S) = \begin{cases} \alpha_{ion} D + \beta_{ion} D^2 & D \leq D_t \\ \alpha_{ion} D_t + \beta_{ion} D_t^2 + (D - D_t) s_{max} & D > D_t \end{cases}$$

$$D_{\mathrm{RBE}} = \begin{cases} \sqrt{-\ln(S)/\beta_{ph} + (\alpha_{ph}/(2\beta_{ph}))^2} - (\alpha_{ph}/(2\beta_{ph})) & -\ln(S) \leq -\ln(S_t) \\ (-\ln(S) + \ln(S_t))/s_{max} + D_t & -\ln(S) > -\ln(S_t) \end{cases} \tag{3.16}$$

where s_{max} is $\alpha_{ph} + 2\beta_{ph} D_t$ and $-\ln(S_t) = \alpha_{ph} D_t + \beta_{ph} D_t^2$ (75).

3.3.4. Modified Microdosimetric Kinetic Model

Japanese light ion facilities use adaptations of the Microdosimetric Kinetic Model (MKM) as their clinically used biophysical models (46; 47). Furthermore, the modified Microdosimetric Kinetic Model (mMKM) has been selected for the first ^{4}He ion therapy using active scanning at HIT (63). Within the mMKM, RBE_α (c.f. equation 3.12) is

$$\mathrm{RBE}_\alpha = 1 + z_{1D}^* \left(\frac{\alpha}{\beta}\right)_{\mathrm{ph}}^{-1}, \tag{3.17}$$

where z_{1D}^* is the saturation-corrected dose-mean specific energy of the domain delivered in a single event, while α_{ph} and β_{ph} are the linear and quadratic terms of the

photon LQ dose response, respectively. In the mMKM, RBE_β is one and a cell is assumed to contain multiple smaller sub-cellular structures called *domains* (46). By approximating a cell with a cylinder of cell radius (R_n) and setting a domain radius (r_d), z^*_{1D} can be calculated with

$$z^*_{1D} = \frac{\int_0^{X_m} z_{sat}(x) z(x) 2\pi \, \mathrm{d}x}{\int_0^{X_m} z(x) 2\pi \, \mathrm{d}x}, \tag{3.18}$$

where X_m is the sum of maximum ion track radius in the Kiefer–Chatterjee model and r_d (46). Both r_d and R_n are free parameters that can be adjusted to tune the mMKM to specific cell types (77). The saturation corrected specific energy (z_{sat}) of a particle can be calculated by

$$z_{sat} = \frac{z_0^2}{z} \left(1 - \exp - \left(\frac{z^2}{z_0^2}\right)\right), \tag{3.19}$$

with the saturation coefficient z_0 (46)

$$z_0 = \frac{(R_n/r_d)^2}{\sqrt{\beta_{ph}(1 + (R_n/r_d)^2}}. \tag{3.20}$$

In this work, z^*_{1D} values for different ion species and energies are calculated as described by Magro et al. (74). Dose averaged values of z^*_{1D} for a mixed radiation field are calculated analogous to $\overline{\alpha}$ (c.f. equation 3.9).

3.4. Monte Carlo Simulations

Historically, MC methods were used to approximate the integral of an function through usage of random numbers when an analytical solution to a function was either analytically impossible to derive or too complex to estimate, e.g. highly multidimensional functions (14). *Enrico Fermi* later extended the MC method to include particle simulations (93). Nowadays, MC simulations are considered the *gold standard* in particle therapy for dose calculation (44).
There are two type of MC simulations: *analog* and *condensed-history* MC simulations (17). Analog MC simulations consider every particle interaction (e.g. single Coulomb scatterings) in a serialised fashion, making it very accurate but also computational heavy, a drawback for clinical applications. Condensed history MC simulations combine multiple small interactions, such as individual Coulomb scattering (c.f. section 2.5) or electronic energy loss (c.f. section 2.1), to a larger interaction. For a large number of interactions (i.e. thick absorbers), this approach is similarly accurate to analog MC simulations, but much faster (17).
There are multiple MC simulation engines that are currently used in particle therapy

(107; 6; 25). At HIT, Fluktuierende Kaskade (FLUKA), a multi-purpose condensed-history MC simulation (30; 9) has been previously established. To improve dose calculation accuracy, the HIT beam-line, as well as other facility parameters were modelled *in-silico* in FLUKA. FLUKA was also used for database generation during facility startup and is extensively benchmarked against measurements (102; 103; 131; 91). Furthermore, the clinically applied biophysical models for ^{12}C ion therapy, LEM and mMKM, were also integrated in FLUKA (75; 74).
Recently, there have been various projects focusing on developing fast MC simulations. To the best of the authors knowledge, only one fastMC simulation for ^{12}C ion therapy exists (108), while all others focus on the much more available (and easier to handle) p therapy (55; 142; 115; 79). In contrast to multi-purpose MC simulations, these fast simulations are clinically viable, meaning their calculation time is usually within minutes and not hours (or even days). However, the improved calculation time is usually accompanied by a loss of generality, as these MC simulations are specifically tailored for particle therapy only.

3.5. Treatment Planning

The goal of radiation therapy is to treat the tumour with a homogeneous dose while completely sparing healthy tissue and Organ at Risk (OAR). As this not realisable with current technology and physics, in the treatment planning process a trade-off is made between target coverage and dose to normal (healthy) tissue, using sophisticated techniques. With Single Field Uniform Dose (SFUD) plans, every field is optimised independently to a homogeneous target dose (52). Contrarily, the Intensity Modulated Particle Therapy (IMPT) technique combines individually in-homogeneous dose fields over multiple entry points to form a homogeneous target dose (73). IMPT was developed analogously to Intensity Modulated Radiation Therapy (IMRT) using photons. Generally, by delivering dose over multiple entry angles, the entrance dose is spread over a larger volume of healthy tissue, reducing the dose to each point. At HIT, patients can be treated with SFUD and IMPT field configurations, based on trade-offs between dose to more normal tissue and target coverage.

3.5.1. The Role of Imaging in Particle Therapy

In clinical practice, despite recent efforts (81; 94), a Computer-Tomography (CT) using X-rays is always required for treatment planning. CT scanners measure the photon absorption coefficient (μ) and reconstruct a three-dimensional image of the patient using multiple radiographies at different angles. As the absolute value of μ for a material (μ_m) can vary with the individual CT scanners, they are normalised

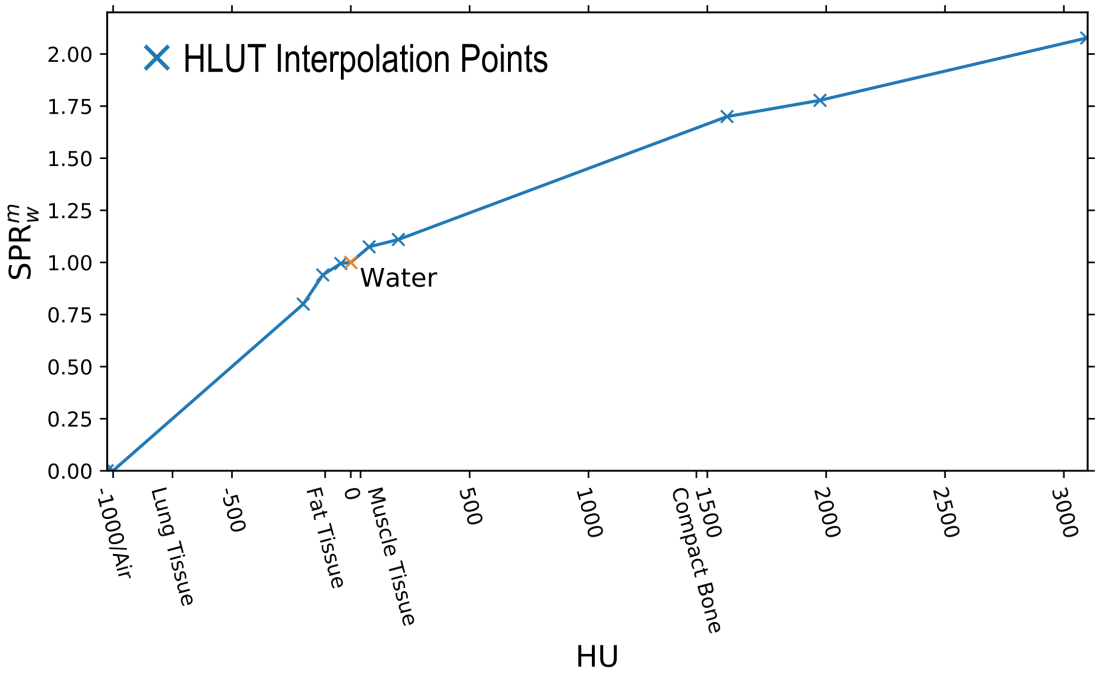

Figure 3.6.: Exemplary HU to SPR_w^m conversion curve that is used for ion beam therapy. HU of different tissue types (120) are indicated on the abscissa.

by μ of water (μ_w) and re-scaled by 1000 (114)

$$\mathrm{HU} = 1000 \cdot \frac{\mu_m - \mu_w}{\mu_w}. \tag{3.21}$$

By definition, HU = 0 corresponds to pure liquid water, while for example HU ~ -1000 and HU ~ 1500 correspond to air/vacuum and cortical bone, respectively (120). Even higher HU values can be found for metal implants in patients. In particle therapy, HU do not linearly correspond to energy loss. To that end, a conversion table that relates HU to energy loss in medium relative to water, i.e. Stopping Power Ratio to Water (SPR_w^m) is required (119). SPR_w^m is defined as

$$\mathrm{SPR}_w^m = \frac{(\mathrm{d}E/\,\mathrm{d}x)_m}{(\mathrm{d}E/\,\mathrm{d}x)_w} \approx \frac{R_m}{R_w}, \tag{3.22}$$

and is approximately the ratio of R_m and R_w, the (remaining) ion ranges in material and water, respectively. Figure 3.6 shows an exemplary HU to SPR_w^m conversion curve. SPR_w^m range from 0.001 in air to around 2 for very high HU of human tissue. The Water Equivalent Thickness (WET) along a straight path dx can then be calculated by integrating the SPR_w^m over the distance

$$\mathrm{WET} = \int \mathrm{SPR}_w^m(x)\,\mathrm{d}x. \tag{3.23}$$

In a voxelised geometry, the integral in equation 3.23 can also be discretised by calculating the intersection between rays and voxels (d_i) and scaling it with the

corresponding $\mathrm{SPR}_{\mathrm{w}}^{\mathrm{m}}(i)$ of the voxel i

$$\mathrm{WET} = \sum_i \mathrm{SPR}_w^m(i) \cdot d_i. \tag{3.24}$$

3.5.2. Dose Optimisation Algorithms

Ignoring OARs and healthy tissue, in the inverse dose-optimisation concept, the goal is to find a beam distribution that homogeneously covers a target with dose. This goal can be formulated by a objective (cost) function F that has to be minimised (13)

$$\min(F) = \min \sum_{i=1}^{M} (D_i - P_i)^2. \tag{3.25}$$

Here D_i and P_i is the current and prescribed dose in voxel i, respectively (13). $\vec{D}$ can be obtained by multiplying the dose-influence-matrix ($\vec{\Lambda}$) with the PB weighting vector $\vec{w}$

$$\vec{\Lambda} \cdot \vec{w} = \vec{D}. \tag{3.26}$$

$\vec{\Lambda}$ is a $M \times N$ matrix containing the dose contributions of N PBs for all M voxels. Figure 3.7 exemplary shows the individual ^{12}C ion dose contributions that form a SOBP.

$$\begin{bmatrix} \overbrace{d_{1,1}}^{\text{PB 1}} & \overbrace{d_{1,2}}^{\text{PB 2}} & \dots & \overbrace{d_{1,N}}^{\text{PB N}} \\ d_{2,1} & d_{2,2} & \dots & d_{2,N} \\ \vdots & \vdots & \ddots & \vdots \\ d_{M-1,1} & d_{M-1,2} & \dots & d_{M-1,N} \\ d_{M,1} & d_{M,2} & \dots & d_{M,N} \end{bmatrix} \cdot \begin{bmatrix} w_1 \\ w_2 \\ \vdots \\ w_{N-1} \\ w_N \end{bmatrix} = \begin{bmatrix} D_1 \\ D_2 \\ \vdots \\ D_{M-1} \\ D_M \end{bmatrix}, \tag{3.27}$$

Using equation 3.26, the objective function can then be written as

$$\min(F) = \min \sum_{i=1}^{M} ((\vec{\Lambda} \cdot \vec{w})_i - P_i)^2. \tag{3.28}$$

For target coverage, an iterative minimisation for the weight of a PB j at the k iteration is given by Lomax et al. using a Newton gradient descent method (84)

$$w_{j,k} = w_{j,k-1} + \left(\sum_{i=1}^{M} d_{i,j}[P_i - D_{i,k-1}] f_{i,j,k-1} \right) / \left(\sum_{i=0}^{M} d_{i,j}^2 \right), \tag{3.29}$$

where the sum is over all M voxels and $f_{i,j,k-1}$ is a damping factor (72). As this method can be applied to every PB independently, this solution is ideal for parallel calculation methods, e.g. with Graphics Processing Units (GPUs) and enables fast dose optimisation (84). F can be extended to also include OARs and other desired quantities such as $\mathrm{D_{RBE}}$, RBE, or cell survival (146; 65; 10; 135).

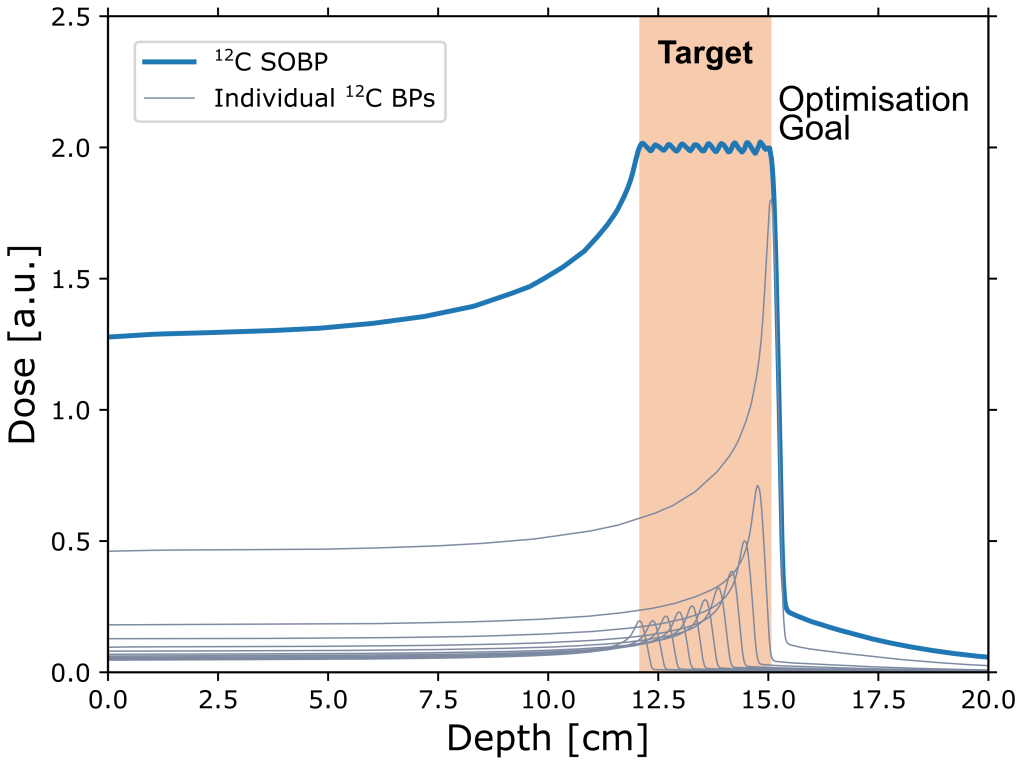

Figure 3.7.: Individual ^{12}C ion BPs that form a SOBP. The optimisation target and goal are displayed.

3.5.3. Plan Robustness

With IMPT, ion beams can nowadays be delivered with millimetre precision to homogeneously irradiate the tumour (73). Nevertheless the treatment outcome can be influenced by small (systematic) variations in the TPS-made physical and biological assumptions, as well as random errors. Uncertainties in particle therapy include, the beam range (up to 4.6 % + 1.2 mm) (98), the patient positioning i.e random setup errors (138), changes in beam delivery, e.g. beam shape ($[-15\,\%, 25\,\%]$ at HIT) (133) and PB targeting, as well as substantial uncertainties to the patient anatomy, such as organ/tumour movement. Nowadays, uncertainties for range and position are mostly considered with extra margins in the target delineation (69) or the treatment planning itself (19; 71). Still, the resulting treatment might not be *robust* under all possible uncertainties. A plan can be considered robust when the treatment outcome is the same, even though the assumptions that were made during the planning process vary slightly. To that end, robust dose optimisation accounting for uncertainties in beam delivery is becoming increasingly available in particle therapy centres (138). Uncertainty scenarios can be accounted for in the cost-functions (c.f. equation 3.25) with additional weighting factors (138). Currently, the most common considered uncertainties in robust optimisation are systematic beam range and patient positioning errors (138).
One way to determine a plan robustness is the so-called *robustness analysis*, where different uncertainty scenarios with an already existing treatment plan are simulated (130). A re-calculation of a plan is usually computational less challenging than an optimisation. Therefore, in a robustness analysis more factors and even the combination of different factors, e.g. changes in the beam shape or beam range together with a positional shift (64), can be simulated potentially yielding a more general overview of the plan robustness. Dose distribution differences to the original plans can be investigated with Dose Volume Histograms (DVHs). DVHs are inverse cumulative histograms of the dose distribution for volumes such as targets and ROIs (118). DVH metrics include the minimum dose D received by $X\%$ of the ROI volume ($D_{X\%}$), a common endpoint in radiation therapy.

3.6. GPU Accelerated Calculations

There are multiple vendors that produce GPUs for computational applications. In this work, only NVIDIA (Santa Clara, CA, USA) in combination with the CUDA C++ toolkit (NVIDIA, Santa Clara, CA, USA) were used. To interlink CUDA to Python applications, the *pycuda* tool was employed (61).
GPUs are pipeline calculation systems that are based on the Single Instruction Multiple Threads (SIMT) execution method to increase calculation throughput by distribution of parallelizable instructions over multiple computational cores. On a GPU, a single instruction, e.g. the addition of two variables, is executed slower than

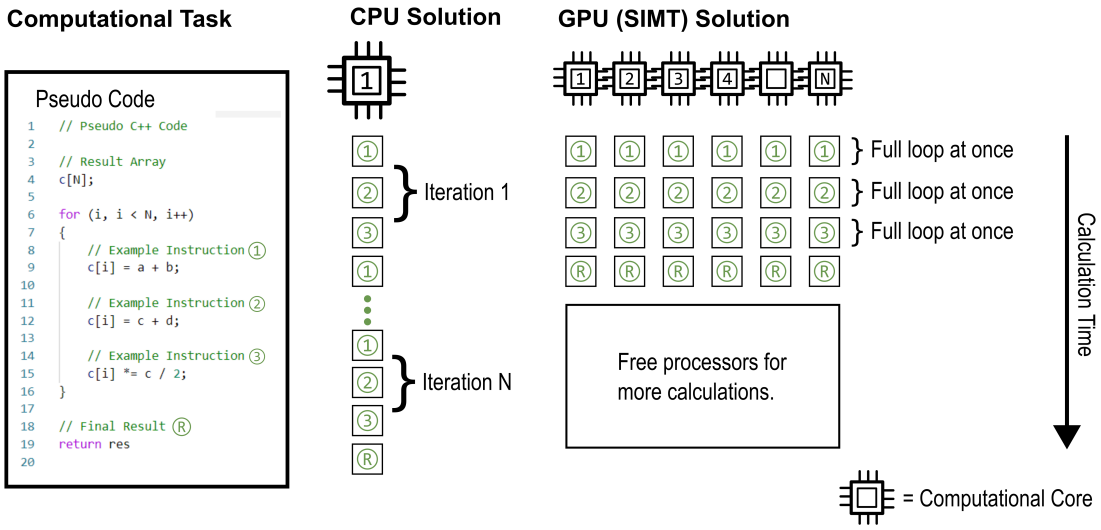

Figure 3.8.: CPU and GPU solutions to a pseudo code task are visualised as a function of calculation time. While the CPU solutions loops over all tasks N times, N GPU processors execute a task at the same time.

on a comparable Central Processing Unit (CPU) (97). Nevertheless the overall computation speed of GPUs is higher than on standard CPUs, as GPUs have far more computational cores. Combined with a very fast and sufficiently large on-board memory, GPUs can achieve high computational performance in dose-calculation and other other suitable tasks (55; 22; 88). Figure 3.8 shows the principal difference between CPUs and GPUs calculations in a simplified fashion. Using a single core, CPUs have to execute the code in a serialised fashion, i.e. a subsequent loop iteration is executed only when the current one is finished. GPUs distribute the instruction loop over multiple computational cores. Figuratively, at the same time-point, all cores execute the same instruction. In reality, on current GPU architectures, a single core can only simultaneously execute a limited amount of threads, while modern CPUs also feature multiple computational cores.
For a first hands-on CUDA with C++, good introductions to NVIDIA CUDA programming have been published on the NVIDIA developer website[a], while a well commented introduction to *pycuda* is also available elsewhere[b]. Furthermore, there is also a detailed handbook for every aspect of CUDA in their latest version[c]. GPU, i.e. parallel thread programming is not intuitive and the errors are often cumbersome to find with *print* functions. The usage of a CUDA debugger such as *cuda-gdb* (an extension of the common C++ gdb debugger[d]) is therefore highly recommended.

[a] https://developer.nvidia.com/blog/even-easier-introduction-cuda/ Accessed 11.2020
[b] https://documen.tician.de/pycuda/tutorial.html, Accessed 01.2021
[c] https://docs.nvidia.com/cuda/cuda-toolkit-release-notes/index.html Accessed 11.2020
[d] https://www.gnu.org/software/gdb/ Accessed: 01.2021

3.7. FRoG

Fast dose Recalculation on GPU (FRoG) is an analytical dose-calculation engine that utilises GPUs for fast and robust dose calculation, as well as other computational tasks. Initially developed in-house at HIT and National Centre for Oncological Hadrontherapy (CNAO) (Pavia, Italy) (111), FRoG is currently also employed at the Varian (Paolo Alto, CA, United States of America) built Danish Centre for Particle Therapy (DCPT) (Aarhus, Denmark) and currently under commissioning at the Normandy Proton Therapy Centre (NPTC) in Caen, France (88; 18; 62). In its current version, FRoGs employs MC simulation generated databases for lateral beam spread parameters in water, Depth-Dose Distribution (DDD), and $\mathrm{LET_d}$. The MC simulations have thereby been tuned to best reproduce facility commissioning and experimental data. FRoG can be called with graphical user interface (GUI) or from the command line, enabling large patient cohort as well as individual case study analysis, respectively. An overview of the FRoG GUI and a FRoG scripting example is provided in appendix A.
In an analytical dose calculation engine, the dose (d) in a voxel (j) with position (x, y) and WET (z), can be calculated by

$$d_j(x_j, y_j, z_j) = \sum_{i=0}^{N} \Phi(\tilde{x_i} - x_j, \tilde{y_i} - y_j, z_j) \cdot \Psi(z_j), \tag{3.30}$$

where the sum is over all N PBs at position (x_i, y_i), Φ describes the dose deposition lateral to the PB, i.e. the lateral beam shape at WET z_j, and Ψ is the DDD in water as a function of WET (45). In FRoG, the lateral beam shape of an pencil beam in water Φ is approximated by either a Triple Gaussian (TG) or Double Gaussian (DG) parameterisation, depending on the treatment facility and Range Shifter (RS) employment (88; 18; 62). To account for the beam shape divergence from the nozzle to the entry into the patient, the lateral spread in water σ_i is convoluted with the initial beam shape at the entrance to the patient (σ_{init}). Φ is therefore described by

$$\Phi(x, y, z) = \sum_{i=0}^{M} w_i \cdot \frac{1}{2\pi(\sigma_{init}^2 + \sigma_i^2(z))} \exp\left(- \frac{x^2 + y^2}{2(\sigma_{init}^2 + \sigma_i^2(z))} \right). \tag{3.31}$$

where M is 2 or 3 for DG or TG beam shape approximations, respectively. Moreover, them sum of all weights w_i is 1 for energy and dose conservation

$$\sum_{i}^{M} w_i = 1. \tag{3.32}$$

In FRoG experimentally determined σ_{init} are used, interpolated by the distance from the nozzle to the patient skin. Currently, FRoG assumes a rotational invariance of the beam shape. To resolve tissue heterogeneities in patients, an individual PB in FRoG is divided in up to 700 sub-PBs. The individual sub-PB has a much smaller Full Width at Half Maximum (FWHM) than the original PB and the weight of

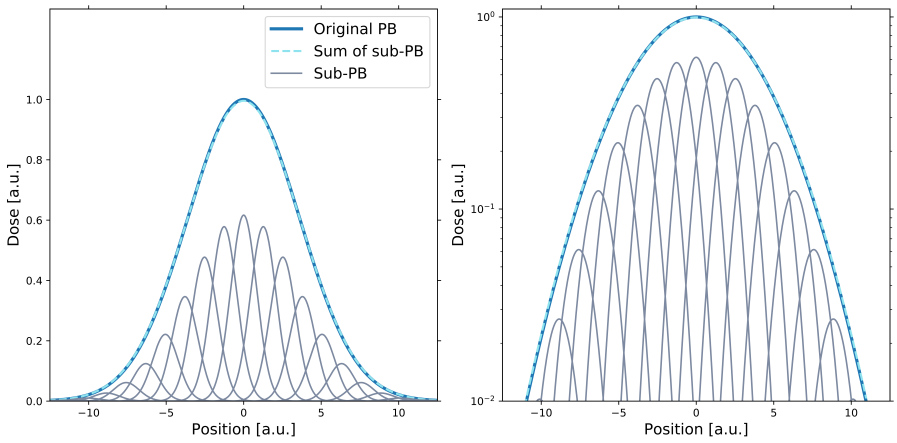

Figure 3.9.: The FRoG PB splitting method is visualised in one-dimension. A pencil beam is divided in multiple sub-PB. The PB is shown on linear (left) and logarithmic (right) scale.

every sub-PB has been chosen so that the superimposition of all sub-PB re-form the original PB (112). Figure 3.9 shows the sub-division of a PB in one-dimensional space. The original beam shape, as well as the individual and sum of sub-spots are displayed on linear and logarithmic scale. Due to the high number of sub-PBs, tissue heterogenities in patients can be accurately resolved (91; 62). In FRoG, the overall calculation time largely depends on the number of PB (correlating with the volume and ion type). Multiple proton RBE models (144; 86; 76) and the LEM and MKM are currently implemented in FRoG. The required biological LQ parameters α and β for these models are calculated for every voxel as described in equation 3.9, where N is the number of PBs. Furthermore, RBE is calculated with equation 3.11 in a post processing step.

For raytracing, FRoG uses a modified *Siddon* stepping algorithm that was specifically tailored for GPU usage (23). Similarly to the original *Siddon* raytracing algorithm, voxel are described by the interception of parallel planes in a Cartesian space (125). However, with the modified *Siddon* stepping algorithm, no merging of relative plane intercepts is required.

By combining FRoG with an external optimiser (10), the *PaRticle thErapy using single and Combined Ion optimization StratEgies* (PRECISE) platform was formed. The PRECISE platform is capable of simultaneously optimising RBE and D_{RBE} homogeneity in the target. In the experimental version of PRECISE, the dose optimisation algorithm has been ported to GPU to increase calculation speed (*Unpublished work of Dr. Eric Heim*).

4. Peer Reviewed Publications

This thesis is presented as a *cumulative thesis* to the Department of Physics and Astronomy of the Heidelberg University, Heidelberg, Germany. The sections 4.A, 4.B, and 4.C have all been published in international peer-reviewed journals. For all three publications, the first author is also the author of this thesis. All publications and selected presentations to international journals and conferences, respectively, are listed in appendix B.

4.A. FRoG: An independent dose and LETd prediction tool for proton therapy at ProBeam® facilities

Authors: Benedikt Kopp, Maria Fuglsang Jensen, Stewart Mein, Lone Hoffmann, Håkan Nyström, Marianne Falk, Thomas Haberer, Amir Abdollahi, Jürgen Debus, and Andrea Mairani
Publication status (7/2020): Published
Journal reference: Medical Physics, 2020, Volume 47, Number 10
DOI: https://doi.org/10.1002/mp.14417

Authors' contributions: BK is the first author of this publication. BK performed all of the presented FRoG computations, carried out the analysis, wrote the main manuscript and constructed all figures. BK extended FRoG to work at cyclotron-based facilities. HN, LH, and SM provided extensive comments to the manuscript. Measurements at DCPT were performed by MFJ, HN, and MF. AM is the lead designer of FRoG and performed MC simulations. BK, SM, and AM are developers of FRoG. TH, AA, and JD provided clinical direction during project development and manuscript writing.

4.B. Rapid effective dose calculation for raster-scanning 4He ion therapy with the modified microdosimetric kinetic model (mMKM)

Authors: Benedikt Kopp, Stewart Mein, Thomas Tessonnier, Judith Besuglow, Semi Harrabi, Eric Heim, Amir Abdollahi, Thomas Haberer, Jürgen Debus, and Andrea Mairani
Publication status (12/2020): Article In Press
Journal reference: Physica Medica: European Journal of Medical Physics, 2020
DOI: https://doi.org/10.1016/j.ejmp.2020.11.028

Authors' contributions: BK is the first author of this publication. BK performed all of the presented computations/analysis and constructed most figures. BK and AM wrote the introduction and method sections of the main manuscript. BK wrote the results, discussion, and conclusion sections of the main manuscript. BK optimised all helium ion plans with PRECISE. The PRECISE optimiser algorithm was ported to GPU by EH with help of BK. Monte Carlo simulated MRFS and bio-tables were generated by AM and SM. TT, JB, and SM provided extensive comments to the manuscript. AM is the lead designer of projects FRoG and PRECISE. BK, SM, and AM are developers of FRoG. SH, TH, AA, and JD provided clinical direction during project development and manuscript writing.

4.C. Development and validation of single field multi-ion particle therapy treatments

Authors: Benedikt Kopp, Stewart Mein, Ivana Dokic, Semi Harrabi, Till Tobias Böhlen, Thomas Haberer, Jürgen Debus, Amir Abdollahi, and Andrea Mairani
Publication status (10/2019): Published
Journal reference: International Journal of Radiation Oncology & Biology & Physics, 2020, Volume 106, Number 1,
DOI: https://doi.org/10.1016/j.ijrobp.2019.10.008

Authors' contributions: BK and SM contributed equally to this publication. BK and SM performed all of the presented computations/analysis, wrote the main manuscript, constructed all figures and realised the experiments. BK developed the PRECISE platform with the base MCTP code TTB provided. BK optimised the investigated patient plans. ID and SM performed biological analysis. AM is the lead designer of projects FRoG and PRECISE. SH, TH, JD, and AA provided clinical direction during project development and manuscript writing.

5. Discussion

5.1. FRoG: A Versatile Tool for Particle Therapy

5.1.1. In Clinical Practice

FRoG is a versatile tool for particle therapy that combines fast dose calculation with MC-like accuracy at HIT and CNAO. After initial verification at both facilities (88; 18), FRoG has been used in recent studies for biological and retrospective clinical research (90). In this work, the FRoG dose algorithm has been extended for cyclotron based calculations, providing third party facilities with an independent tool to investigate $\mathrm{LET_d}$ and variable RBE of their treatment plans (136). Independence between primary TPS and secondary re-calculation tools can reduce the risk of calculation errors. For instance, different approaches in beam shape modelling can lead to different dose predictions in the patient. The current TPS at HIT Syngo (Siemens, Erlangen, Germany) uses a DG beam shape approximation (146), while FRoG uses a TG approximation (88). Therefore, if two independent calculation methods yield the same dosimetric result, it is more probable that the dose predictions hold true. Nevertheless, underlying delivery, range, and position uncertainties could still influence the treatment outcome. To that end, independent robustness analysis (as is implemented in FRoG) can be a vital clinical tool as has been shown in publication 4.A. Additionally, FRoG implementations for calculation methods (e.g. CT to $\mathrm{SPR_w^m}$ conversion) and analysis metrics (e.g. DVH calculation) provide an additional level of independence to the clinically used TPSs.
The FRoG splitting algorithm was tested in this work using a heterogeneous head phantom, yielded good agreement to measurements. These findings are in line recent studies that also showed good agreement to measurements and MC simulations (91). Consequently, it can be assumed that FRoG's pencil beam splitting algorithm combined with a TG/DG (c.f. section 3.7) beam shape approximation is applicable at most active-scanning particle therapy facilities.
Determination of RBE for p and other ions is one of the most important current challenges in particle therapy (99; 134), as it can directly impact the treatment outcome. As every facility can employ different approaches of prescription dose, treatment schedule, and beam angles to minimise dose and $\mathrm{LET_d}$ in OARs, the comparability of treatment results is additionally clouded. Using the physical and biological dose calculation kernels that are currently implemented in FRoG, treatment facilities,

like the DCPT, now have a fast and versatile method to independently verify and crosscheck their treatment plans for e.g. RBE, D_{RBE}, and LET_d. With FRoG recalculations, plans that show high RBE variation, or are not robust can be exposed and if necessary re-planned.
Using the dose kernel for cyclotron accelerated particle beams developed in this work, FRoG is currently being commissioned at the Normandy Proton Therapy Centre (NPTC) in Caen, France. So far, at NPTC, patients are treated with p only, but plans are currently underway to also establish ^{12}C ion therapy in Caen (105). As FRoG's pencil beam algorithm is universally applicable for all ion species and now also all accelerator types, the benefits that the FRoG platform provides for p could also directly be used for their ^{12}C ion therapy project, providing secondary dose calculation during facility commissioning and clinical startup.

5.1.2. The Future of FRoG

The combination of FRoG with an Mixed Radiation Field Spectra (MRFS) has extended the use cases of FRoG even further. Besides the derivation of biological FRoG-databases from the MRFS as introduced in this work, MRFS could also be coupled with particle specific cross-sections, modelling the production of γ-rays or positrons for position emission tomography. Combined with the possibility to extend FRoG for online-dose calculation, these data could be employed for in-treatment patient verification. A similar online-dose calculation project has been carried out in a recent work, also using a fast dose calculation engine (33).
Despite great success in homogeneous and heterogeneous conditions, FRoG's analytical dose kernel is still limited in accuracy by its approximations, assumptions, and databases. To accurately predict the dose in patients with a RS employment, multiple databases with different RS to skin distances had to be created. On the other hand, multi-purpose MC codes can specifically simulate the RS as an additional geometry in the beam path. The resulting particle scattering from the RS as well as the beam divergence in the air-gap between RS and patient are only limited by the physics assumptions in the MC simulations and the *in-silico* experiment modelling. However, multi-purpose MC simulations are confined by their calculation time. Although, recent efforts produced fast MC engines with clinically relevant time scales, they are mostly limited to p beams (55; 142; 115; 79). Therefore, FRoG's dose calculation engine will also be relevant for future clinical use until fast MC are also available for other all light ions that are currently used or are intended for clinical usage, namely ^{4}He, ^{12}C, and ^{16}O ions. Furthermore, these MC codes should yield similar or better accuracy, flexibility, and calculation times as FRoG. When the previously mentioned requirements are met, the analytical dose kernel should be replaced with a MC driven algorithm.
While MC simulations using a dedicated CPU cluster take several hours to calculate one patient, FRoG yields similar dose, LET_d, and RBE predictions within minutes

(88). At HIT, large scale retrospective patient analysis are feasible with FRoG and currently underway to e.g. evaluate the LET_d distribution with Chordoma as a function of beam setup and tumour volume. The findings that these analyses provide could ultimately help to adjust/modify patient prescription as well as reveal secondary treatment goals that cause increased tumour control, such as minimum LET_d (40; 82).

5.1.3. The PRECISE Platform

All plans that were investigated in publications 4.B and 4.C were created with the PRECISE platform. The adaptation of new models and methods, e.g. ^{4}He-mMKM treatment plans and Multi-Ion Therapy (MIT)/Combined Ion-Beam with Constant RBE (CICR) therapy plans could have only be realised due to FRoG's and PRECISE's flexible design, i.e the simple and fast realisation of new calculation methods. The PRECISE platform is thereby paving the way for the translation of novel methods and treatments to clinical practice. Nevertheless, the optimiser architecture is currently limited by the amount and quality of cost-functions that are available. For treatment plans investigated in this work, emphasis was put on target coverage, dose in OARs, and in the case of CICR fields RBE homogeneity. With adapted OAR and target cost functions using a clinically viable optimisation strategy, the resulting treatment plans should therefore be even more conformal. Nevertheless, the PRECISE platform could also be an integral part of a patient specific treatment planning regime, that quickly creates and compares potential treatment plans with different ions. PRECISE could also be used for online-therapy, where the dose is calculated with FRoG on the fly during a treatment and the dose re-optimised with PRECISE to match dose prescriptions.

5.2. Novel Techniques in Particle Therapy

5.2.1. Helium Ion Beam Therapy with Active Scanning

Uncertainties of RBE with mMKM

RBE is one of the most elusive quantity in particle therapy. RBE varies with the prescribed dose, X-ray dose response, i.e. tissue (or cell) type, expected cell survival level, and calculation method. However, to exploit the $\sim$ 100 years of clinical experience with X-rays, RBE is also an essential variable in particle therapy and there are various mechanistic as well as phenomenological models that try to relate biological effects of light ions to photons (41; 28; 46; 144; 86; 76). Since initial clinical experience with ^{12}C ion at GSI, LEM has been the clinically applied bio-physical dose model for RBE prediction in Europe (36; 21; 134). With the revival of ^{4}He ion beam

therapy using active scanning, for the first time mMKM will be used to predict RBE distributions at HIT. To that end, RBE uncertainties with mMKM under clinical parameters has been investigated in publication 4.B. The importance of the X-ray LQ parameter β_{ph} was compared for two dose levels that are under consideration for clinical startup. Considerable differences in target dose were observed when varying the absolute values of β_{ph} from $0.0025\,\text{Gy}^{-2}$ to $0.0250\,\text{Gy}^{-2}$. However, the variations in β_{ph} were also found to be less important than changes in $(\alpha/\beta)_{\text{ph}}$ for mMKM in the investigated dose range. Despite that, for ^{12}C ion beam therapy at HIT, a LQ X-ray response of 2 Gy is usually assumed for normal and cancer tissue. To that end, FRoG could be employed to investigate the treatment plans for RBE uncertainties assuming different radio-sensitivities for the tumour. Treatment plans that show high uncertainties could be flagged and potentially re-planned using different biological assumptions or field configurations.

Remaining Challenges

Besides α_{ph} (or $(\alpha/\beta)_{\text{ph}}$), mMKM uses three parameters to predicted the expected cell survival, i.e. determine the RBE. In this work, best fit values from literature (77) were used for the cell and domain radius in publication 4.B for mMKM RBE prediction. With a fixed $(\alpha/\beta)_{\text{ph}}$ and cell/domain radius, the only free parameter that can be chosen in mMKM is the quadratic photon dose response within the LQ model, i.e. β_{ph}. Currently, for ^{12}C ion beam therapy at HIT, a β_{ph} value of $0.05\,\text{Gy}^{-2}$ is used for clinical practice. However, the final choice of β_{ph} for actively scanned ^{4}He ion therapy with mMKM should also be subjected to the assumptions of the LQ model. For a typical tumour dose $2\,\text{Gy}_{\text{RBE}}$ and $3\,\text{Gy}_{\text{RBE}}$ per fraction, a β of $0.05\,\text{Gy}^{-2}$ with an $(\alpha/\beta)_{\text{ph}} = 2\,\text{Gy}$ leads to expected cell survivals of $\sim 67\,\%$ and $\sim 47\,\%$, respectively. Using the lower bound of β_{ph} ($0.0025\,\text{Gy}^{-2}$) from publication 4.B, the same dosage yields cell survival levels that are $\sim 96\,\%$. Applying a previously used Tumor Control Probability (TCP) model (135) based on Poission statistics and assuming a tumour volume of $\sim 4\,\text{cm}^3$ as well as a cell density of $10^4\,/\text{mm}^3$, for an β_{ph} of $0.05\,\text{Gy}^{-2}$, 50 % of tumour control is achieved in between 70 to $90\,\text{Gy}_{\text{RBE}}$. Similarly, using the lower bound of β_{ph} that was investigated in publication 4.B, the same dose and fractionation yields a TCP of $\sim 0\,\%$. Although the chosen TCP model is a first order approximation that neglects variable radio-sensitivity and cell density in the tumour, which increases TCP values (118), the values here are in strong contrast to the clinically observed treatment outcome of e.g. chordoma tumours. At GSI, five year local tumour control probabilities for chordoma were $> 70\,\%$ with a median dose of $60\,\text{Gy}_{\text{RBE}}$ and $3\,\text{Gy}_{\text{RBE}}$ per fractions ^{12}C ion therapy (137). Therefore, very low values of β_{ph} seem improbable under the LQ and the TCP model. However, Van Leeuven et al. reviewed the β_{ph} from patient cohort analyses of various tumour sites and found β_{ph} in the range from $0.001 - 0.06\,\text{Gy}^{-2}$ (139). Nevertheless, in the expected dose regime of $\sim 3\,\text{Gy}_{\text{RBE}}$, higher values of β_{ph} would satisfy both, the assumptions in the LQ model and the range of previously

found β_{ph} values. To build on previous experience at HIT, an $(\alpha/\beta)_{\mathrm{ph}}$ of 2 Gy could be used for clinical startup, while afterwards tumour specific values, e.g. 2.45 Gy for Chordoma (42) would further personalise the tumour treatment. Regardless of the final biological assumption, the choice of β_{ph} and $(\alpha/\beta)_{\mathrm{ph}}$ should be thoroughly investigated before clinical practice.

FRoG for Independent mMKM Verification

For the first commercial TPS for ^{4}He ion beam therapy with active scanning at HIT, a MRFS approach will be used to predict RBE. Compared to MC simulations, that explicitly considers the biological effect of every particle, an in energy and depth finitely spaced MRFS by definition marginalises the mixed radiation field. However, the observed differences between full MC generated databases and MRFS derived were clinically acceptable. Nevertheless, additional efforts should investigate the impact of depth and energy spacing on RBE prediction accuracy. If the same dose difference between MC simulated and MRFS derived databases could be achieved with a coarser MRFS binning, the calculation time could be further reduced and potentially the complete MRFS instead of databases could be transported in FRoG. For initial clinical startup of ^{4}He ion beam therapy, FRoG will function as an independent dose calculation engine to the commercial RayStation TPS (RaySearch Laborathories, Stockholm, Sweden). RayStation generated treatment plans are going to be forward calculated with FRoG and interdependently verified. Additionally, model sensitivity studies could be performed, similar to the ones presented in this work. Through the independent verification with FRoG, I) the risk of dose-calculation errors are minimised and II) physicians gain insight on important secondary metrics such as $\mathrm{LET_d}$ that FRoG also provides with every dose calculation. Additional to the independent plan verification, FRoG could also be used for *in-silico* Quality Assurance (QA) at HIT, where treatment plan consistency is verified by two independent calculation engines rather than by experimental validation. As patient specific QA is a time consuming part of the clinical workflow that blocks sparsely available machine capacities, *in-silico* instead of dosimetric QA could further increase the patient throughput (83).

5.2.2. Multi-ion Beam Therapy

Combined Ion Beam Therapy with Constant RBE

All ions that are currently used for particle therapy have distinctive strengths and weaknesses. ^{12}C and higher Z ions feature high $\mathrm{LET_d}$ distributions in the patient that are favourable to overcome hypoxic tumour conditions (32) as well as a sharp lateral penumbra due to reduced Coulomb scattering. Nevertheless, all light ions with $Z > 1$ are also accompanied by a fragmentation tail which extends over the

BP and potentially delivers dose to healthy tissue. p have a finite range in the patient, making them especially suited in treatments with OARs at the distal edge of the tumour, but undergo enhanced lateral scattering compared to high Z ions. Furthermore, the biological effectiveness and LET of p is lowest of all light ions. In this work CICR treatments that combine multiple ions in the same treatment field to yield an almost homogeneous RBE and therefore physical dose distributions were developed. The idea of MIT is not new and has been previously proposed to homogenise or to boost LET_d as well as provide a constant RBE in the target (48; 127; 11). In this work, these studies were extended upon by creating CICR fields with combinations of ^{12}C ions with ^{4}He ions and p. CICR plans were optimised for three patient cases using the PRECISE platform and showed increased RBE and physical dose homogeneity compared to ^{12}C ion therapy. In the dose optimisation, no weight was given LET_d homogeneity. Nevertheless, more uniform LET_d were found in the target for CICR plans compared to ^{12}C ion plans. Therefore, LET_d homogeneity of CICR plans is correlated to the RBE homogeneity, even though LET_d alone is not a good predictor for RBE (RBE depends on the LET spectrum of all particles in the mixed radiation field) (37). Additionally, $CICR_{C-p}$ fields featured reduced surrounding dose compared to single ion p plans and increased biological stability under tissue uncertainties/biophysical models compared to fields with single ions (with the exception of p fields that showed the highest biologically stable dose distributions). For these reasons, CICR fields could be employed in clinical practice to reduce the uncertainties in RBE that are currently intrinsic to light ion therapy and provide a conformal treatment option.

Current Challenges

Worldwide, the application of ^{12}C ion therapy is limited due to the increased technical complexity compared to p therapy and high facility startup cost. In 2018, there were 12 ion beam therapy centres with a ^{12}C ion therapy, of which two thirds were in Japan and the remaining in Europe (134). Out of the 12 centres, only two employ a gantry that can deliver ions other than p, limiting the degrees of freedom for plan delivery (39; 54). Nevertheless, interest in light ion therapy with $Z > 1$ is increasing (68; 78). This is essential for the progress of MIT, as a limited number of ^{12}C ion facilities also limits the amount of patients that could benefit from MIT. Furthermore, a low number of patients could potentially lead to problems of statistical verification of treatment outcomes with MIT.
Besides structural challenges, MIT also faces new uncertainties during delivery of CICR treatments. In this work, the individual branches of MIT plans were delivered in sequence after another. While sufficient for fixed phantoms and treatments of stereotactic tumours, the sequential irradiation of different ion branches is a potential source of uncertainty in clinical application that adds to the overall delivery uncertainty. Intrafractional organ or tumour movement in the patient could lead to a distorted ion mixing, potentially yielding a reduced physical dose and therefore

RBE homogeneity in the target. To reduce this effect, two potential strategies could be employed:

A) multiple ion delivery in the same beam spill and

B) fast switching between ion sources.

The mixture of multiple ions in the same spill has been also theorised and investigated in previous works for treatment positioning verification (85; 141) and to modify the RBE of ions (57), respectively. While perfectly suited for range verification, as the range of ions is proportional to A/Z^2 and for particle acceleration in a synchrotron, ions in the same spill should have similar momentum per nucleon, magnetic rigidity, and (A/Z) (85), there are only few possible options (e.g. t and $^3He^+$) where ions could be delivered in the same spill and reach the same depth in the patient. Fast switching between ion sources therefore seems like a better prospect to decrease uncertainties from intrafractional tumour movement. Different ion species would be delivered quickly after another on the same scanning spot positions, which reduces time dependent delivery uncertainties. If treatment indications with large intrafractional variations such as observable in lung tumours could be treated with CICR fields should be closely investigated though. Besides MIT, fast ion switching techniques could also be employed for other purposes, such as range verification in particle therapy as proposed in a recent work (141).
As with every other particle species, CICR plans might not be applicable for all tumour types and indications. To illustrate this fact, figure 5.1 schematically shows three potential treatment scenarios with a fixed beam direction; a target is accompanied by none (case I), distally surrounding (case II), or proximal OARs (case III). For single field configurations, case II would be more challenging for CICR treatments, especially for CICR plans with p as the most distal branch, since the large lateral scattering from p as well as the tail from higher Z ions would contribute to normal tissue dose. The additional complexity of a RBE homogeneity in the TPS optimisation, could lead to a trade-off between, RBE, target coverage, and normal tissue dose, as can be seen in publication 4.C supplementary figure 1. Here novel concepts such as ion arc therapy (26; 92) could potentially reduce the normal tissue dose compared to single ion SFUD or IMPT plans. Contrarily to case II, case I and III could benefit from the physical aspects of $CICR_{C-p}$ treatments. The proximal OARs are spared from the highly scattering p contribution and the tail dose of higher Z ions would not directly hit critical tissue. Additional plan comparison studies that investigate the normal tissue dose and target conformity should be performed before clinical practice using state of the art optimisers.

Future Directions of MIT

In a novel experiment using both a homogeneous and anthropomorphic phantom, the biological efficacy of MIT has been experimentally verified in this work for one

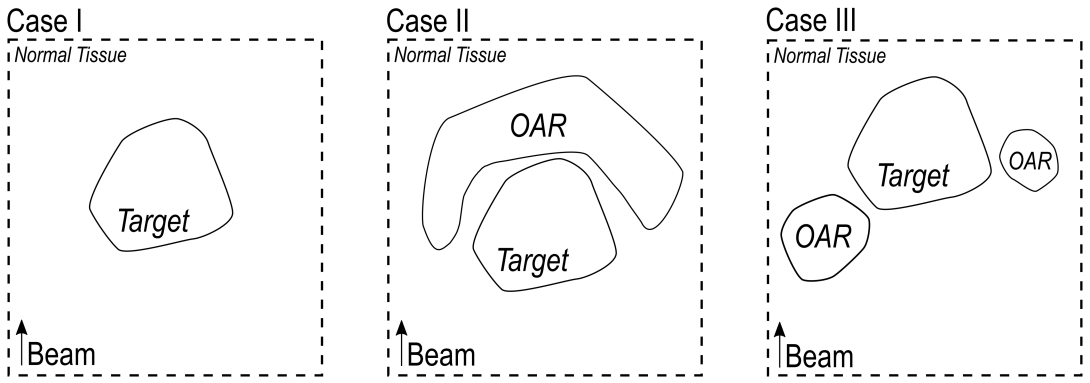

Figure 5.1.: Three potential tumour positions with no OAR (case I), distally surrounding (case II), and lateral proximal (case III) are displayed. Case I and III are better suited for $\mathrm{CICR}_{\mathrm{C}-p}$ treatments, while for II target coverage and RBE homogeneity could be limited by normal tissue dose. For case II, SFUD, IMPT, or ARC plans using only one particle species might be the best solution to spare normal tissue.

cell line, yielding good agreement to predictions. Additionally, the biological stability of CICR and single ion SFUD plans has been investigated *in-silico* for one patient and two biological models, showing that CICR fields can produce a similar biological stability as p. In a future effort, these *in-silico* predictions could be verified with further experiments. For one cell line optimised CICR fields could be simultaneously delivered on cell lines with different radio-sensitivities. In more biologically robust treatment plans, the cell survival should be independent on the tumour depth, i.e. homogeneous in the target. Furthermore, such an experiment is in first approximation similar to the clinical experience at HIT, where tumours are usually treated with a constant biological assumption, i.e. fixed $(\alpha/\beta)_{\mathrm{ph}}$ and β_{ph}.

So far only single field configurations of CICR treatments were investigated in this work. Single field configurations are the most challenging types of field configurations to create a constant RBE distribution in the target. The physical dose distribution has to be optimised so that the different ion species homogenise the biological effect. Following the methodology of IMPT, CICR fields could be delivered from multiple angles to spread out the dose over more tissue. The combination of ^{12}C and ^{4}He in a single CICR field has shown small gradients in the RBE distributions. However, opposing field IMPT configurations with ^{12}C and ^{4}He ions already show an increased homogeneous physical dose distribution compared to single fields. High LET ions from one beam are automatically mixed with low LET ions from the other. To that end, investigations if multi-field CICR plans with only high Z particles could provide a more homogeneous RBE distribution in the target than in a single field configuration should be performed.

The concept of CICR treatments could be extended to also include volume independent constant RBE (VICR), which was realised *in-silico* a previous work (11) using opposing field configurations. To achieve VICR fields in a single field arrangement, depending on the WET in beam direction, different ion species could be matched to deliver a constant physical dose in the target. As in a single field configuration the degrees of freedom are lower than for multiple field arrangements, the choice of ions will play a more important role. For small WET, low Z particles such as p or ^{4}He ions with relatively low biological efficacy can be combined, while for large WET high Z particles would be required to yield constant RBE. With VICR therapy, the prescription to a tumour could be again physical dose (and potentially $\mathrm{LET_d}$), reducing the number of uncertainties that are accompanied in RBE calculation by one dimension.
Despite all the advantages that MIT and especially CICR could provide, as has been shown here, further research has to be performed and technologies must be developed for CICR treatments to reach clinical practice.

6. Summary

Three publications in international peer reviewed journals have been put forward, detailing the development and verification of new evaluation methods and treatment options for particle therapy to reduce uncertainties.
FRoG has been extended from a software that was specifically tailored to two synchrotron based sister-facilities (CNAO and HIT) to also be employed at third party cyclotron-facilities in publication 4.A. There, FRoG has been established as a secondary dose engine to independently recalculate patient treatments and provide additional information, such as variable p RBE and $\mathrm{LET_d}$. The FRoG dose algorithm was tested against measurements in a homogeneous and heterogeneous, i.e. anthropomorphic setting, yielding excellent results. Additionally, FRoG calculations for ten patient plans that were delivered at DCPT were compared against the clinically employed TPS. For one patient, a widely applied p RBE model was used to calculate the variable RBE distribution, revealing the potential of state of the art secondary dose calculation engines for clinical practice. With FRoG, daily clinical checks on RBE and $\mathrm{LET_d}$ as well as large scale retrospective patient analysis can be performed in a clinical time frame (minutes/patient (88)). Further, third party facilities obtained a tool to independently very their dose predictions and gain insight on additional clinically relevant quantities, potentially increasing patient treatment conformity. Additionally, FRoG dose calculations could also be used instead of patient specific QA, *in-silico* verifying treatment plans before patient treatment.
A new method in FRoG that uses MRFS derived databases for ^{4}He ion $\mathrm{D_{RBE}}$ calculation with the mMKM was developed in publication 4.B. As a similar MRFS approach will be used in the first clinically used TPS of ^{4}He ions with active scanning, the dose difference was compared against the original FRoG calculation method, yielding clinically acceptable agreements. Furthermore, to provide a reference for the upcoming choice of β_{ph} of the clinically anticipated biophysical RBE model (mMKM), the influence of β_{ph} on the overall biological dose distribution was investigated for two potential clinical values. Although substantial differences were observed between both β_{ph} values, additional investigations with changes in $(\alpha/\beta)_{\mathrm{ph}}$ showed greater differences, leading to the conclusion that $(\alpha/\beta)_{\mathrm{ph}}$ is the most important factor in mMKM for the investigated dose range and should be generally chosen with care. With the new MRFS implementation, FRoG will be used as an independent secondary dose calculation engine for the clinically used TPS at HIT during the starting phase of clinical trials. By analysing RBE sensitivity and $\mathrm{LET_d}$ distributions for every patient, FRoG is paving the way for the successful translation

of a novel treatment modality to clinical practice.
The development and validation of single field MIT therapy was presented in publication 4.C. By combining multiple ion species in the same treatment field, homogeneous physical dose and RBE distribution can be achieved. The experimental CICR treatment plans were delivered at the HIT and biologically and dosimetrically verified in a homogeneous and heterogeneous phantom. Additional single field CICR treatment plans were optimised for three patients. The biological stability under different assumptions was investigated, yielding similarly high biological stability as p while decreasing dose to surrounding normal tissue for combinations of p and ^{12}C ions in the same treatment field. CICR treatments were also found to feature more homogeneous $\mathrm{LET_d}$ distributions than comparing ^{12}C ion treatment plans. Novel techniques such as CICR greatly expand the catalogue of treatment options for cancer patients, potentially improving patient outcome in the future.
In this work, new models, techniques and methods were presented that evaluate and reduce the uncertainties accompanied with particle therapy. With FRoG, treatment plans can now be independently verified for QA, while the biological uncertainty of a newly applied biophysical model was investigated for ^{4}He beam therapy. Furthermore, with CICR plans, a potential biologically robust multi-ion treatment option was developed and experimentally verified.

Appendices

A. Additional Information to FRoG

Figure A.1 shows the graphical user interface in FRoG.

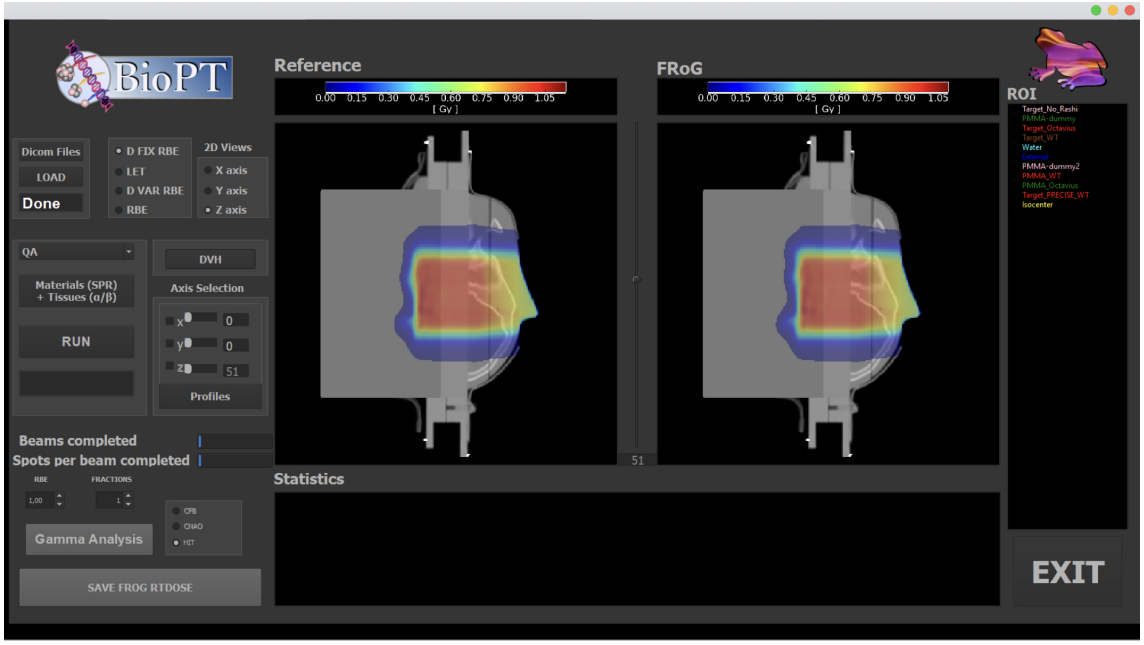

Figure A.1.: The FRoG graphical user interface is displayed. Figure taken from Mein (87).

In the following a commented FRoG example script is shown. The paths to files and folders have been replaced with generic values.

```
#!/usr/bin/python
##########################################
# Name: scripting_FRoG_example.py        #
# SCRIPTING EXAMPLE FOR FROG HIT         #
# Benedikt Kopp January 2021             #
##########################################

# To catch argument values etc.
import sys

# To check if files exist
# and to make directories
import os

# Append FRoG directory to the
# Python search path
frog_path = '/path/to/FROG/' # Replace with path to FRoG
sys.path.insert(0, frog_path)

# Export FRoG Path
os.environ['frog'] = frog_path

# From the main FRoG file
# import the FROG_class which
# which has all the FRoG functions
# and dose calculation.
from FROG import FROG_class

# Function to crawl through dicoms/files/folders
from glob import glob

# Example script
# that runs a single
# FRoG Calculation
def main_SingleRun():
    ###################################
    # Begin Initialisation
    ###################################

    ###################################
    # Save Dicoms
    ###################################
    savepath = '/dev/null' # Specify folder to path

    # Check if path exists
    if not os.path.exists(savepath):
        try:
            os.mkdir(savepath)
        except:
            print "Could not create folder"
            return -1

    # Initiate an instance of the FROG_class
    # Notice the False argument which disables the GUI
    FRoG = FROG_class(False)

    # Load the FRoG configuartion for HIT
    FRoG.HIT_Config(True)

    # Link the CT File to FRoG
    ct_file = '/home/HIT/Data/HIT_Patients/CTFILE.dcm'    # Note: CT files should be in their own folder
    FRoG.Dicom_load.ct_clicked_main(ct_file, isGUI=False) # isGUI keyword used to supress Graphical Interface

    # Link the RTPLAN File to FRoG
    pl_file = '/home/HIT/Data/HIT_Patients/RTPLAN.dcm'
    FRoG.Dicom_load.pl_clicked_main(pl_file, isGUI=False)

    # Link the Structure Set to FRoG
    st_file = '/home/HIT/Data/HIT_Patients/STRUCT.dcm'
    FRoG.Dicom_load.st_clicked_main(st_file, isGUI=False)

    # Link a Reference Dose File to FRoG
    ds_file = '/home/HIT/Data/HIT_Patients/DOSE.dcm'
    FRoG.Dicom_load.ds_clicked_main(ds_file, isGUI=False)

    # Load the STRUCT, Dose, Plan, CT into FRoG
    FRoG.exec_clicked()

    ###################################
    # Begin Dose Calculation
    ###################################
    FRoG.Dose_cal_TG_clicked()

```

```
84      ###################################
85      # DVH Calculation
86      ###################################
87      _, dvh_dataset = FRoG.dvhcal_clicked()
88
89      # dvh_dataset will have the following structure/keys:
90      # 'ROI Name'  : List of ROI Names
91      # 'D_2%'      : List of calculated DVH Metric D2%
92      # 'D_5%'      : List of calculated DVH Metric D5%
93      # 'D_50%'     : List of calculated DVH Metric D50%
94      # 'D_95%'     : List of calculated DVH Metric D95%
95      # 'D_98%'     : List of calculated DVH Metric D98%
96      # 'Dose max'  : List of maximum Dose in ROI
97      # 'Dose Mean' : List of mean Dose in ROI
98      # 'Dose'      : List of np.arrays with dose
99      # 'Volume'    : List of np.arrays with corresponding volume
100     # 'STD'       : List of standard deviation in the ROI
101     # 'Color'     : List of color coding in the ROI - RGB
102     # Note: The order of the list is defined by the ROI Name List
103
104     # Function to save the RTDose Files
105     FRoG.dosedcmsave_clicked()
106
107     os.rename("Files","%s/Files" % savepath)
108
109     # Since we moved the FILES folder to savepath a new one is created
110     os.mkdir("Files")
111
112     ###################################
113     # Delete FRoG Object
114     #
115     # This cleans the FRoG object
116     # and makes sure that there are no
117     # class values left
118     ###################################
119     del FRoG
120
121     return 0
122
123 # Python convention on starting the
124 # main script
125 if __name__ == "__main__":
126     main_SingleRun()
```

B. List of Publications

Manuscripts

Kopp, B., Mein, S., Tessonnier, T., Besuglow, J., Harrabi, S., Heim, E., ... & Mairani, A. (2020). Rapid effective dose calculation for raster-scanning 4He ion therapy with the modified microdosimetric kinetic model (mMKM). Physica Medica: European Journal of Medical Physics.
This publication has been used for this thesis.

Kopp, B., Fuglsang Jensen, M., Mein, S., Hoffmann, L., Nyström, H., Falk, M., ... & Mairani, A. (2020). FRoG: An independent dose and LETd prediction tool for proton therapy at ProBeam® facilities. Medical Physics.
This publication has been used for this thesis.

Mein, S., Klein, C., **Kopp, B.**, Magro, G., Harrabi, S., Karger, C. P., ... & Mairani, A. (2020). Assessment of RBE-weighted dose models for carbon ion therapy towards modernization of clinical practice at HIT: in vitro, in vivo and in patients. International Journal of Radiation Oncology* Biology* Physics.

Kopp, B., Mein, S., Dokic, I., Harrabi, S., Böhlen, T. T., Haberer, T., ... & Mairani, A. (2020). Development and validation of single field multi-ion particle therapy treatments. International Journal of Radiation Oncology* Biology* Physics, 106(1), 194-205.
This publication has been used for this thesis.

Mein, S., **Kopp, B.**, Tessonnier, T., Ackermann, B., Ecker, S., Bauer, J., ... & Debus, J. (2019). Dosimetric validation of Monte Carlo and analytical dose engines with raster-scanning 1H, 4He, 12C, and 16O ion-beams using an anthropomorphic phantom. Physica Medica, 64, 123-131.

Choi, K., Mein, S. B., **Kopp, B.**, Magro, G., Molinelli, S., Ciocca, M., & Mairani, A. (2018). FRoG—A new calculation engine for clinical investigations with proton and carbon ion beams at CNAO. Cancers, 10(11), 395.

Mein, S., Choi, K., **Kopp, B.**, Tessonnier, T., Bauer, J., Ferrari, A., ... & Mairani, A. (2018). Fast robust dose calculation on GPU for high-precision 1 H, 4 He, 12 C and 16 O ion therapy: The FRoG platform. Scientific reports, 8(1), 1-12.

Selected Conference Presentations

Kopp, B., Mein, S., Choi, K., Bauer, J., Debus, J., and Mairani, A., (2019) FRoG (Fast dose Recalculation on GPU) at the Heidelberg Ion-Beam Therapy Center, Oral Presentation, *International Conference on the Use of Computers in Radiation Therapy (ICCR), Montreal, Canada.*

Bibliography

[1] Adeberg, S., Harrabi, S. B., Verma, V., Bernhardt, D., Grau, N., Debus, J., and Rieken, S. Treatment of meningioma and glioma with protons and carbon ions. *Radiation oncology 12*, 1 (2017), 1–7. 15

[2] Ahlen, S. P. Theoretical and experimental aspects of the energy loss of relativistic heavily ionizing particles. *Reviews of Modern Physics 52*, 1 (1980), 121. 10

[3] Astrahan, M. Some implications of linear-quadratic-linear radiation dose-response with regard to hypofractionation. *Medical physics 35*, 9 (2008), 4161–4172. 21

[4] Ballarini, F., Biaggi, M., Edwards, A., Ferrari, A., Ottolenghi, A., Pelliccioni, M., and Scannicchio, D. Estimating mixed field effects: an application supporting the lack of a non-linear component for chromosome aberration induction by neutrons. *Radiation protection dosimetry 103*, 1 (2003), 19–27. 17, 19

[5] Batey, M. A., Zhao, Y., Kyle, S., Richardson, C., Slade, A., Martin, N. M., Lau, A., Newell, D. R., and Curtin, N. J. Preclinical evaluation of a novel atm inhibitor, ku59403, in vitro and in vivo in p53 functional and dysfunctional models of human cancer. *Molecular cancer therapeutics 12*, 6 (2013), 959–967. 19

[6] Battistoni, G., Bauer, J., Boehlen, T. T., Cerutti, F., Chin, M. P., Dos Santos Augusto, R., Ferrari, A., Ortega, P. G., Kozłowska, W., Magro, G., et al. The fluka code: an accurate simulation tool for particle therapy. *Frontiers in oncology 6* (2016), 116. 23

[7] Bauer, J., Sommerer, F., Mairani, A., Unholtz, D., Farook, R., Handrack, J., Frey, K., Marcelos, T., Tessonnier, T., Ecker, S., et al. Integration and evaluation of automated monte carlo simulations in the clinical practice of scanned proton and carbon ion beam therapy. *Physics in Medicine & Biology 59*, 16 (2014), 4635. 7

[8] Belli F. Cera R. Cherubini M. Dalla Vecchia Ami Haque F. Ianzini G. Moschini O. Sapora G. Simone Ma Tabocchini P. Tiveron, M. RBE-LET relationships for cell inactivation and mutation induced by low energy protons in v79 cells:

further results at the lnl facility. *International Journal of Radiation Biology 74*, 4 (1998), 501–509. 19

[9] Böhlen, T., Cerutti, F., Chin, M., Fassò, A., Ferrari, A., Ortega, P. G., Mairani, A., Sala, P. R., Smirnov, G., and Vlachoudis, V. The fluka code: developments and challenges for high energy and medical applications. *Nuclear data sheets 120* (2014), 211–214. 23

[10] Böhlen, T. T., Bauer, J., Dosanjh, M., Ferrari, A., Haberer, T., Parodi, K., Patera, V., and Mairani, A. A monte carlo-based treatment-planning tool for ion beam therapy. *Journal of radiation research 54*, suppl_1 (2013), i77–i81. 25, 30

[11] Böhlen, T. T., Brons, S., Dosanjh, M., Ferrari, A., Fossati, P., Haberer, T., Patera, V., and Mairani, A. Investigating the robustness of ion beam therapy treatment plans to uncertainties in biological treatment parameters. *Physics in Medicine & Biology 57*, 23 (2012), 7983. 82, 85

[12] Bohr, N. Scattering and stopping of fission fragments. *Physical Review 58*, 7 (1940), 654. 10

[13] Bortfeld, T., Bürkelbach, J., Boesecke, R., and Schlegel, W. Methods of image reconstruction from projections applied to conformation radiotherapy. *Physics in Medicine & Biology 35*, 10 (1990), 1423. 25

[14] Caflisch, R. E., et al. Monte carlo and quasi-monte carlo methods. *Acta numerica 1998* (1998), 1–49. 22

[15] Carabe, A., Moteabbed, M., Depauw, N., Schuemann, J., and Paganetti, H. Range uncertainty in proton therapy due to variable biological effectiveness. *Physics in Medicine & Biology 57*, 5 (2012), 1159. 9

[16] Chatterjee, A., and Schaefer, H. Microdosimetric structure of heavy ion tracks in tissue. *Radiation and environmental biophysics 13*, 3 (1976), 215–227. 17

[17] Chetty, I. J., Curran, B., Cygler, J. E., DeMarco, J. J., Ezzell, G., Faddegon, B. A., Kawrakow, I., Keall, P. J., Liu, H., Ma, C.-M. C., et al. Report of the aapm task group no. 105: Issues associated with clinical implementation of monte carlo-based photon and electron external beam treatment planning. *Medical physics 34*, 12 (2007), 4818–4853. 22

[18] Choi, K., Mein, S. B., Kopp, B., Magro, G., Molinelli, S., Ciocca, M., and Mairani, A. Frog—a new calculation engine for clinical investigations with proton and carbon ion beams at cnao. *Cancers 10*, 11 (2018), 395. 29, 77

[19] Chu, M., Zinchenko, Y., Henderson, S. G., and Sharpe, M. B. Robust optimization for intensity modulated radiation therapy treatment planning under uncertainty. *Physics in Medicine & Biology 50*, 23 (2005), 5463. 27

[20] Chu, W., Ludewigt, B., and Renner, T. Instrumentation for treatment of cancer using proton and light-ion beams. *Review of Scientific Instruments 64*, 8 (1993), 2055–2122. 14

[21] Combs, S. E., Jäkel, O., Haberer, T., and Debus, J. Particle therapy at the heidelberg ion therapy center (hit)–integrated research-driven university-hospital-based radiation oncology service in heidelberg, germany. *Radiotherapy and Oncology 95*, 1 (2010), 41–44. 2, 21, 79

[22] Da Silva, J., Ansorge, R., and Jena, R. Sub-second pencil beam dose calculation on gpu for adaptive proton therapy. *Physics in Medicine & Biology 60*, 12 (2015), 4777. 28

[23] De Greef, M., Crezee, J., Van Eijk, J., Pool, R., and Bel, A. Accelerated ray tracing for radiotherapy dose calculations on a gpu. *Medical physics 36*, 9Part1 (2009), 4095–4102. 30

[24] Demtröder, W. *Experimentalphysik 4*. Springer Berlin Heidelberg, 2017. 13, 14

[25] Deng, W., Younkin, J. E., Souris, K., Huang, S., Augustine, K., Fatyga, M., Ding, X., Cohilis, M., Bues, M., Shan, J., et al. Integrating an open source monte carlo code "mcsquare" for clinical use in intensity-modulated proton therapy. *Medical physics 47*, 6 (2020), 2558–2574. 23

[26] Ding, X., Li, X., Zhang, J. M., Kabolizadeh, P., Stevens, C., and Yan, D. Spot-scanning proton arc (sparc) therapy: the first robust and delivery-efficient spot-scanning proton arc therapy. *International Journal of Radiation Oncology* Biology* Physics 96*, 5 (2016), 1107–1116. 83

[27] Elsässer, T., Krämer, M., and Scholz, M. Accuracy of the local effect model for the prediction of biologic effects of carbon ion beams in vitro and in vivo. *International Journal of Radiation Oncology* Biology* Physics 71*, 3 (2008), 866–872. 21

[28] Elsässer, T., and Scholz, M. Cluster effects within the local effect model. *Radiation research 167*, 3 (2007), 319–329. 3, 79

[29] Elsässer, T., Weyrather, W. K., Friedrich, T., Durante, M., Iancu, G., Krämer, M., Kragl, G., Brons, S., Winter, M., Weber, K.-J., et al. Quantification of the relative biological effectiveness for ion beam radiotherapy: direct experimental comparison of proton and carbon ion beams and a novel approach for treatment planning. *International Journal of Radiation Oncology* Biology* Physics 78*, 4 (2010), 1177–1183. 21

[30] Ferrari, A., Sala, P. R., Fasso, A., Ranft, J., Siegen, U., et al. Fluka: a multi-particle transport code. Tech. rep., Stanford Linear Accelerator Center (SLAC), 2005. 23

[31] Fowler, J. F. The linear-quadratic formula and progress in fractionated radiotherapy. *The British journal of radiology 62*, 740 (1989), 679–694. 19

[32] Furusawa, Y., Fukutsu, K., Aoki, M., Itsukaichi, H., Eguchi-Kasai, K., Ohara, H., Yatagai, F., Kanai, T., and Ando, K. Inactivation of aerobic and hypoxic cells from three different cell lines by accelerated 3he-, 12c-and 20ne-ion beams. *Radiation research 154*, 5 (2000), 485–496. 19, 81

[33] Giordanengo, S., Vignati, A., Attili, A., Ciocca, M., Donetti, M., Fausti, F., Manganaro, L., Milian, F., Molinelli, S., Monaco, V., et al. Ridos: A new system for online computation of the delivered dose distributions in scanning ion beam therapy. *Physica Medica 60* (2019), 139–149. 78

[34] Goitein, M. *Radiation oncology: a physicist's-eye view*. Springer Science & Business Media, 2007. 1, 2, 7, 9

[35] Gottschalk, B. On the scattering power of radiotherapy protons. *Medical physics 37*, 1 (2010), 352–367. 11

[36] Grün, R., Friedrich, T., Elsässer, T., Krämer, M., Zink, K., Karger, C., Durante, M., Engenhart-Cabillic, R., and Scholz, M. Impact of enhancements in the local effect model (lem) on the predicted rbe-weighted target dose distribution in carbon ion therapy. *Physics in Medicine & Biology 57*, 22 (2012), 7261. 79

[37] Grün, R., Friedrich, T., Traneus, E., and Scholz, M. Is the dose-averaged let a reliable predictor for the relative biological effectiveness? *Medical physics 46*, 2 (2019), 1064–1074. 82

[38] Haberer, T., Becher, W., Schardt, D., and Kraft, G. Magnetic scanning system for heavy ion therapy. *Nuclear Instruments and Methods in Physics Research Section A: Accelerators, Spectrometers, Detectors and Associated Equipment 330*, 1-2 (1993), 296–305. 14

[39] Haberer, T., Debus, J., Eickhoff, H., Jäkel, O., Schulz-Ertner, D., and Weber, U. The heidelberg ion therapy center. *Radiotherapy and Oncology 73* (2004), S186–S190. 15, 16, 82

[40] Hagiwara, Y., Bhattacharyya, T., Matsufuji, N., Isozaki, Y., Takiyama, H., Nemoto, K., Tsuji, H., and Yamada, S. Influence of dose-averaged linear energy transfer on tumour control after carbon-ion radiation therapy for pancreatic cancer. *Clinical and Translational Radiation Oncology 21* (2020), 19–24. 79

[41] Hawkins, R. B. A microdosimetric-kinetic theory of the dependence of the rbe for cell death on let. *Medical physics 25*, 7 (1998), 1157–1170. 3, 79

[42] Henderson, F. C., McCool, K., Seigle, J., Jean, W., Harter, W., and Gagnon, G. J. Treatment of chordomas with cyberknife: georgetown university experience and treatment recommendations. *Neurosurgery 64*, suppl_2 (2009), A44–A53. 81

[43] Highland, V. L. Some practical remarks on multiple scattering. *Nuclear Instruments and Methods 129*, 2 (1975), 497–499. 11

[44] Hissoiny, S., Ozell, B., Bouchard, H., and Després, P. Gpumcd: a new gpu-oriented monte carlo dose calculation platform. *Medical physics 38*, 2 (2011), 754–764. 22

[45] Hong, L., Goitein, M., Bucciolini, M., Comiskey, R., Gottschalk, B., Rosenthal, S., Serago, C., and Urie, M. A pencil beam algorithm for proton dose calculations. *Physics in Medicine & Biology 41*, 8 (1996), 1305. 29

[46] Inaniwa, T., Furukawa, T., Kase, Y., Matsufuji, N., Toshito, T., Matsumoto, Y., Furusawa, Y., and Noda, K. Treatment planning for a scanned carbon beam with a modified microdosimetric kinetic model. *Physics in Medicine & Biology 55*, 22 (2010), 6721. 3, 21, 22, 79

[47] Inaniwa, T., and Kanematsu, N. Adaptation of stochastic microdosimetric kinetic model for charged-particle therapy treatment planning. *Physics in Medicine & Biology 63*, 9 (2018), 095011. 21

[48] Inaniwa, T., Kanematsu, N., Noda, K., and Kamada, T. Treatment planning of intensity modulated composite particle therapy with dose and linear energy transfer optimization. *Physics in Medicine & Biology 62*, 12 (2017), 5180. 82

[49] International Commission on Radiation Units and Measurements. *ICRU Report 49: Stopping powers and ranges for protons and alpha particles*. International commission on radiation units and measurements, 1993. 5, 16

[50] International Commission on Radiation Units and Measurements. *ICRU Report 60: Fundamental Quantities and Units for Ionizing Radiation*. International commission on radiation units and measurements, 1998. 6

[51] International Commission on Radiation Units and Measurements. *ICRU Report 90: Key Data for Ionizing-Radiation Dosimetry: Measurement Standards and Applications*. International commission on radiation units and measurements, 2014. 5

[52] International Commission on Radiation Units and Measurements. *ICRU REPORT 93: Prescribing, Recording, and Reporting Light Ion Beam Therapy*. International commission on radiation units and measurements, 2016. 5, 8, 9, 11, 14, 23

[53] Ito, A., Nakano, H., Kusano, Y., Hirayama, R., Furusawa, Y., Murayama, C., Mori, T., Katsumura, Y., and Shinohara, K. Contribution of indirect action to radiation-induced mammalian cell inactivation: dependence on photon energy and heavy-ion let. *Radiation research 165*, 6 (2006), 703–712. 17

[54] Iwata, Y., Fujita, T., Fujimoto, T., Furukawa, T., Hara, Y., Kondo, K., Mizushima, K., Murakami, T., Muramatsu, M., Nishiuchi, M., et al. Development of carbon-ion radiotherapy facilities at nirs. *IEEE Transactions on Applied Superconductivity 28*, 3 (2017), 1–7. 15, 82

[55] Jia, X., Schümann, J., Paganetti, H., and Jiang, S. B. Gpu-based fast monte carlo dose calculation for proton therapy. *Physics in Medicine & Biology 57*, 23 (2012), 7783. 23, 28, 78

[56] Jongen, Y., Abs, M., Blondin, A., Kleeven, W., Zaremba, S., Vandeplassche, D., Aleksandrov, V., Gursky, S., Karamyshev, O., Karamysheva, G., et al. Compact superconducting cyclotron c400 for hadron therapy. *Nuclear Instruments and Methods in Physics Research Section A: Accelerators, Spectrometers, Detectors and Associated Equipment 624*, 1 (2010), 47–53. 13

[57] Kanai, T., Furusawa, Y., Fukutsu, K., Itsukaichi, H., Eguchi-Kasai, K., and Ohara, H. Irradiation of mixed beam and design of spread-out bragg peak for heavy-ion radiotherapy. *Radiation research 147*, 1 (1997), 78–85. 83

[58] Karger, C. P., Peschke, P., Sanchez-Brandelik, R., Scholz, M., and Debus, J. Radiation tolerance of the rat spinal cord after 6 and 18 fractions of photons and carbon ions: experimental results and clinical implications. *International Journal of Radiation Oncology* Biology* Physics 66*, 5 (2006), 1488–1497. 3, 21

[59] Kellerer, A. M., and Rossi, H. H. The theory of dual radiation action. *Current Topics in Radiation Research Quarterly* (1974), 85–158. 17

[60] Kiefer, J., and Straaten, H. A model of ion track structure based on classical collision dynamics (radiobiology application). *Physics in Medicine & Biology 31*, 11 (1986), 1201. 17

[61] Klöckner, A., Pinto, N., Lee, Y., Catanzaro, B., Ivanov, P., and Fasih, A. Pycuda and pyopencl: A scripting-based approach to gpu run-time code generation. *Parallel Computing 38*, 3 (2012), 157–174. 27

[62] Kopp, B., Fuglsang Jensen, M., Mein, S., Hoffmann, L., Nyström, H., Falk, M., Haberer, T., Abdollahi, A., Debus, J., and Mairani, A. Frog: An independent dose and letd prediction tool for proton therapy at probeam® facilities. *Medical Physics 47*, 10 (2020), 5274–5286. 29, 30

[63] Kopp, B., Mein, S., Tessonnier, T., Besuglow, J., Harrabi, S., Heim, E., Abdollahi, A., Haberer, T., Debus, J., and Mairani, A. Rapid effective dose calculation for raster-scanning 4he ion therapy with the modified microdosimetric kinetic model (mmkm). *Physica Medica: European Journal of Medical Physics* (2020). 21

[64] Kraan, A. C., van de Water, S., Teguh, D. N., Al-Mamgani, A., Madden, T., Kooy, H. M., Heijmen, B. J., and Hoogeman, M. S. Dose uncertainties in impt for oropharyngeal cancer in the presence of anatomical, range, and setup errors. *International Journal of Radiation Oncology* Biology* Physics 87*, 5 (2013), 888–896. 27

[65] Krämer, M., and Scholz, M. Treatment planning for heavy-ion radiotherapy: calculation and optimization of biologically effective dose. *Physics in Medicine & Biology 45*, 11 (2000), 3319. 25

[66] Krieger, H. *Grundlagen der Strahlungsphysik und des Strahlenschutzes*, 6. auflage ed. Springer eBook Collection. Springer Spektrum, Berlin ; [Heidelberg], 2019. 17

[67] Kurz, C. *4D offline PET-based treatment verification in ion beam therapy. Experimental and clinical evaluation*. PhD thesis, 2014. 9

[68] Laine, A., Pompos, A., Story, M., Jiang, S., Timmerman, R., and Choy, H. International symposium on ion therapy: Planning the first hospital-based heavy ion therapy center in the united states. *International journal of particle therapy 2*, 3 (2015), 468–471. 82

[69] Landberg, T., Chavaudra, J., Dobbs, J., Gerard, J. P., Hanks, G., Horiot, J. C., Johansson, K. A., Möller, T., Purdy, J., Suntharalingam, N., and Svensson, H. Icru report 62: Prescribing, recording and reporting photon beam therapy (supplement to icru report 50). *Journal of the International Commission on Radiation Units and Measurements os32*, 1 (Nov. 1999), 3–20. 27

[70] Liew, H., Klein, C., Zenke, F. T., Abdollahi, A., Debus, J., Dokic, I., and Mairani, A. Modeling the effect of hypoxia and dna repair inhibition on cell survival after photon irradiation. *International journal of molecular sciences 20*, 23 (2019), 6054. 19

[71] Liu, W., Zhang, X., Li, Y., and Mohan, R. Robust optimization of intensity modulated proton therapy. *Medical physics 39*, 2 (2012), 1079–1091. 27

[72] Lomax, A. Intensity modulation methods for proton radiotherapy. *Physics in Medicine & Biology 44*, 1 (1999), 185. 25

[73] Lomax, A., Boehringer, T., Coray, A., Egger, E., Goitein, G., Grossmann, M., Juelke, P., Lin, S., Pedroni, E., Rohrer, B., et al. Intensity modulated proton therapy: a clinical example. *Medical Physics 28*, 3 (2001), 317–324. 23, 27

[74] Magro, G., Dahle, T., Molinelli, S., Ciocca, M., Fossati, P., Ferrari, A., Inaniwa, T., Matsufuji, N., Ytre-Hauge, K., and Mairani, A. The fluka monte carlo code coupled with the nirs approach for clinical dose calculations in carbon ion therapy. *Physics in Medicine & Biology 62*, 9 (2017), 3814. 22, 23

[75] Mairani, A., Brons, S., Cerutti, F., Fasso, A., Ferrari, A., Krämer, M., Parodi, K., Scholz, M., and Sommerer, F. The fluka monte carlo code coupled with the local effect model for biological calculations in carbon ion therapy. *Physics in Medicine & Biology 55*, 15 (2010), 4273. 21, 23

[76] Mairani, A., Dokic, I., Magro, G., Tessonnier, T., Bauer, J., Böhlen, T., Ciocca, M., Ferrari, A., Sala, P., Jäkel, O., et al. A phenomenological relative biological effectiveness approach for proton therapy based on an improved description of the mixed radiation field. *Physics in Medicine & Biology 62*, 4 (2017), 1378. 3, 7, 30, 79

[77] Mairani, A., Magro, G., Tessonnier, T., Böhlen, T., Molinelli, S., Ferrari, A., Parodi, K., Debus, J., and Haberer, T. Optimizing the modified microdosimetric kinetic model input parameters for proton and 4he ion beam therapy application. *Physics in Medicine & Biology 62*, 11 (2017), N244. 22, 80

[78] Malouff, T. D., Mahajan, A., Krishnan, S., Beltran, C., Seneviratne, D. S., and Trifiletti, D. M. Carbon ion therapy: A modern review of an emerging technology. *Frontiers in oncology 10* (2020), 82. 82

[79] Maneval, D., Ozell, B., and Després, P. pgpumcd: an efficient gpu-based monte carlo code for accurate proton dose calculations. *Physics in Medicine & Biology 64*, 8 (2019), 085018. 23, 78

[80] Martins, P. M., Dal Bello, R., Ackermann, B., Brons, S., Hermann, G., Kihm, T., and Seco, J. Pibs: Proton and ion beam spectroscopy for in vivo measurements of oxygen, carbon, and calcium concentrations in the human body. *Scientific Reports 10*, 1 (2020), 1–14. 15

[81] Maspero, M., Van den Berg, C. A., Landry, G., Belka, C., Parodi, K., Seevinck, P. R., Raaymakers, B. W., and Kurz, C. Feasibility of mr-only proton dose calculations for prostate cancer radiotherapy using a commercial pseudo-ct generation method. *Physics in Medicine & Biology 62*, 24 (2017), 9159. 23

[82] Matsumoto, S., Lee, S. H., Imai, R., Inaniwa, T., Matsufuji, N., Fukahori, M., Kohno, R., Yonai, S., Okonogi, N., Yamada, S., et al. Unresectable chondrosarcomas treated with carbon ion radiotherapy: Relationship between dose-averaged linear energy transfer and local recurrence. *Anticancer Research 40*, 11 (2020), 6429–6435. 79

[83] Matter, M., Nenoff, L., Meier, G., Weber, D. C., Lomax, A. J., and Albertini, F. Alternatives to patient specific verification measurements in proton therapy: a comparative experimental study with intentional errors. *Physics in Medicine & Biology 63*, 20 (2018), 205014. 81

[84] Matter, M., Nenoff, L., Meier, G., Weber, D. C., Lomax, A. J., and Albertini, F. Intensity modulated proton therapy plan generation in under ten seconds. *Acta oncologica 58*, 10 (2019), 1435–1439. 25

[85] Mazzucconi, D., Agosteo, S., Ferrarini, M., Fontana, L., Lante, V., Pullia, M., and Savazzi, S. Mixed particle beam for simultaneous treatment and online range verification in carbon ion therapy: Proof-of-concept study. *Medical physics 45*, 11 (2018), 5234–5243. 83

[86] McNamara, A. L., Schuemann, J., and Paganetti, H. A phenomenological relative biological effectiveness (rbe) model for proton therapy based on all published in vitro cell survival data. *Physics in Medicine & Biology 60*, 21 (2015), 8399. 3, 7, 30, 79

[87] Mein, S. *FRoG: a fast robust analytical dose engine on GPU for p, 4He, 12C and 16O particle therapy*. PhD thesis, Heidelberg University Faculty of Physics and Astronomy, 2020. 15, 91

[88] Mein, S., Choi, K., Kopp, B., Tessonnier, T., Bauer, J., Ferrari, A., Haberer, T., Debus, J., Abdollahi, A., and Mairani, A. Fast robust dose calculation on gpu for high-precision 1 h, 4 he, 12 c and 16 o ion therapy: The frog platform. *Scientific reports 8*, 1 (2018), 1–12. 28, 29, 77, 79, 87

[89] Mein, S., Dokic, I., Klein, C., Tessonnier, T., Böhlen, T. T., Magro, G., Bauer, J., Ferrari, A., Parodi, K., Haberer, T., et al. Biophysical modeling and experimental validation of relative biological effectiveness (rbe) for 4 he ion beam therapy. *Radiation Oncology 14*, 1 (2019), 123. 3

[90] Mein, S., Klein, C., Kopp, B., Magro, G., Harrabi, S., Karger, C. P., Haberer, T., Debus, J., Abdollahi, A., Dokic, I., et al. Assessment of rbe-weighted dose models for carbon ion therapy towards modernization of clinical practice at hit: in vitro, in vivo and in patients. *International Journal of Radiation Oncology* Biology* Physics* (2020). 21, 77

[91] Mein, S., Kopp, B., Tessonnier, T., Ackermann, B., Ecker, S., Bauer, J., Choi, K., Aricò, G., Ferrari, A., Haberer, T., et al. Dosimetric validation of monte carlo and analytical dose engines with raster-scanning 1h, 4he, 12c, and 16o ion-beams using an anthropomorphic phantom. *Physica Medica 64* (2019), 123–131. 2, 23, 30, 77

[92] Mein, S., Tessonnier, T., Kopp, B., Harrabi, S., Abdollahi, A., Debus, J., Haberer, T., and Mairani, A. Spot-scanning hadron arc (sharc) therapy: a

study with light and heavy ions. Under Review in: Advances in Radiation Oncology, 2021. 83

[93] Metropolis, N. The beginning. *Los Alamos Science 15* (1987), 125–130. 22

[94] Meyer, S., Kamp, F., Tessonnier, T., Mairani, A., Belka, C., Carlson, D. J., Gianoli, C., and Parodi, K. Dosimetric accuracy and radiobiological implications of ion computed tomography for proton therapy treatment planning. *Physics in Medicine & Biology 64*, 12 (2019), 125008. 23

[95] Moliere, G. Theorie der streuung schneller geladener teilchen i. einzelstreuung am abgeschirmten coulomb-feld. *Zeitschrift für Naturforschung A 2*, 3 (1947), 133–145. 11

[96] Moliere, G. Theorie der streuung schneller geladener teilchen ii mehrfach-und vielfachstreuung. *Zeitschrift für Naturforschung A 3*, 2 (1948), 78–97. 11

[97] NVIDIA Corporation. Programming Guide cuda toolkit documentation. https://docs.nvidia.com/cuda/cuda-c-programming-guide/index.html. Section 1: Introduction; Accessed: 2021-01-07. 28

[98] Paganetti, H. Range uncertainties in proton therapy and the role of monte carlo simulations. *Physics in Medicine & Biology 57*, 11 (2012), R99. 27

[99] Paganetti, H., Blakely, E., Carabe-Fernandez, A., Carlson, D. J., Das, I. J., Dong, L., Grosshans, D., Held, K. D., Mohan, R., Moiseenko, V., et al. Report of the aapm tg-256 on the relative biological effectiveness of proton beams in radiation therapy. *Medical physics 46*, 3 (2019), e53–e78. 3, 19, 77

[100] Paganetti, H., Niemierko, A., Ancukiewicz, M., Gerweck, L. E., Goitein, M., Loeffler, J. S., and Suit, H. D. Relative biological effectiveness (rbe) values for proton beam therapy. *International Journal of Radiation Oncology* Biology* Physics 53*, 2 (2002), 407–421. 19

[101] Parodi, K. *On the feasibility of dose quantification with in-beam PET data in radiotherapy with {sup 12} C and proton beams.* PhD thesis, Fakultät Mathematik und Naturwissenschaften der Technischen Universität Dresden, 2004. 11

[102] Parodi, K., Mairani, A., Brons, S., Hasch, B.-G., Sommerer, F., Naumann, J., Jäkel, O., Haberer, T., and Debus, J. Monte carlo simulations to support start-up and treatment planning of scanned proton and carbon ion therapy at a synchrotron-based facility. *Physics in Medicine & Biology 57*, 12 (2012), 3759. 16, 23

[103] Parodi, K., Mairani, A., and Sommerer, F. Monte carlo-based parametrization of the lateral dose spread for clinical treatment planning of scanned proton and

carbon ion beams. *Journal of radiation research 54*, suppl_1 (2013), i91–i96. 23

[104] Particle Therapy Co-Operative Group. Ptcog - facilities in operation. https://ptcog.ch/index.php/facilities-in-operation. Accessed: 2021-01-21. 1

[105] Particle Therapy Co-Operative Group. Ptcog - facilities under construction. https://ptcog.ch/index.php/facilities-under-construction. Accessed: 2021-01-27. 78

[106] Pedroni, E., Bacher, R., Blattmann, H., Böhringer, T., Coray, A., Lomax, A., Lin, S., Munkel, G., Scheib, S., Schneider, U., et al. The 200-mev proton therapy project at the paul scherrer institute: Conceptual design and practical realization. *Medical physics 22*, 1 (1995), 37–53. 14

[107] Perl, J., Shin, J., Schümann, J., Faddegon, B., and Paganetti, H. Topas: an innovative proton monte carlo platform for research and clinical applications. *Medical physics 39*, 11 (2012), 6818–6837. 23

[108] Qin, N., Pinto, M., Tian, Z., Dedes, G., Pompos, A., Jiang, S. B., Parodi, K., and Jia, X. Initial development of gocmc: a gpu-oriented fast cross-platform monte carlo engine for carbon ion therapy. *Physics in Medicine & Biology 62*, 9 (2017), 3682. 23

[109] Röntgen, W. C. Über eine neue art von strahlen. *Sitzungsber. Phys. Medi. Gesellsch. Würzburg 1* (1885), 132–141. 1

[110] Rossi, B. B. *High-energy particles*. Prentice-Hall, 1952. 10

[111] Rossi, S. The status of cnao. *The European Physical Journal Plus 126*, 8 (2011), 78. 29

[112] Russo, G., Attili, A., Battistoni, G., Bertrand, D., Bourhaleb, F., Cappucci, F., Ciocca, M., Mairani, A., Milian, F., Molinelli, S., et al. A novel algorithm for the calculation of physical and biological irradiation quantities in scanned ion beam therapy: the beamlet superposition approach. *Physics in Medicine & Biology 61*, 1 (2015), 183. 30

[113] Saager, M., Glowa, C., Peschke, P., Brons, S., Grün, R., Scholz, M., Huber, P. E., Debus, J., and Karger, C. P. The relative biological effectiveness of carbon ion irradiations of the rat spinal cord increases linearly with let up to 99 kev/μm. *Acta Oncologica 55*, 12 (2016), 1512–1515. 3

[114] Schardt, D., Elsässer, T., and Schulz-Ertner, D. Heavy-ion tumor therapy: Physical and radiobiological benefits. *Reviews of modern physics 82*, 1 (2010), 383. 1, 2, 6, 7, 8, 9, 10, 11, 13, 15, 16, 17, 24

[115] Schiavi, A., Senzacqua, M., Pioli, S., Mairani, A., Magro, G., Molinelli, S., Ciocca, M., Battistoni, G., and Patera, V. Fred: a gpu-accelerated fast-monte carlo code for rapid treatment plan recalculation in ion beam therapy. *Physics in Medicine & Biology 62*, 18 (2017), 7482. 23, 78

[116] Schipler, A., and Iliakis, G. Dna double-strand–break complexity levels and their possible contributions to the probability for error-prone processing and repair pathway choice. *Nucleic acids research 41*, 16 (2013), 7589–7605. 17

[117] Schippers, J., Dölling, R., Duppich, J., Goitein, G., Jermann, M., Mezger, A., Pedroni, E., Reist, H., Vrankovic, V., et al. The sc cyclotron and beam lines of psi's new protontherapy facility proscan. *Nuclear Instruments and Methods in Physics Research Section B: Beam Interactions with Materials and Atoms 261*, 1-2 (2007), 773–776. 13

[118] Schlegel, W., Karger, C. P., and Jäkel, O. *Medizinische Physik: Grundlagen–Bildgebung–Therapie–Technik*. Springer-Verlag, 2018. 1, 9, 11, 13, 17, 27, 80

[119] Schneider, U., Pedroni, E., and Lomax, A. The calibration of ct hounsfield units for radiotherapy treatment planning. *Physics in Medicine & Biology 41*, 1 (1996), 111. 24

[120] Schneider, W., Bortfeld, T., and Schlegel, W. Correlation between ct numbers and tissue parameters needed for monte carlo simulations of clinical dose distributions. *Physics in Medicine & Biology 45*, 2 (2000), 459. 24

[121] Scholz, M. Effects of ion radiation on cells and tissues. In *Radiation effects on polymers for biological use*. Springer, 2003, pp. 95–155. 18

[122] Schömers, C., Feldmeier, E., Galonska, M., Haberer, T., Horn, J., Peters, A., et al. First tests of a re-accelerated beam at heidelberg ion-beam therapy centre (hit). In *8th Int. Particle Accelerator Conf.(IPAC'17), Copenhagen, Denmark, 14â 19 May, 2017* (2017), JACOW, Geneva, Switzerland, pp. 4647–4649. 14

[123] Schulz-Ertner, D., Karger, C. P., Feuerhake, A., Nikoghosyan, A., Combs, S. E., Jäkel, O., Edler, L., Scholz, M., and Debus, J. Effectiveness of carbon ion radiotherapy in the treatment of skull-base chordomas. *International Journal of Radiation Oncology* Biology* Physics 68*, 2 (2007), 449–457. 21

[124] Serber, R. Nuclear reactions at high energies. *Physical Review 72*, 11 (1947), 1114. 7

[125] Siddon, R. L. Fast calculation of the exact radiological path for a three-dimensional ct array. *Medical physics 12*, 2 (1985), 252–255. 30

[126] Siegel, R. L., Miller, K. D., and Jemal, A. Cancer statistics, 2020. *CA: A Cancer Journal for Clinicians 70*, 1 (2020), 7–30. 1

[127] Sokol, O., Krämer, M., Hild, S., Durante, M., and Scifoni, E. Kill painting of hypoxic tumors with multiple ion beams. *Physics in Medicine & Biology 64*, 4 (2019), 045008. 82

[128] Spinelli, A., and Pellino, G. Covid-19 pandemic: perspectives on an unfolding crisis. *The British journal of surgery* (2020). 1

[129] Stewart, R. D., Carlson, D. J., Butkus, M. P., Hawkins, R., Friedrich, T., and Scholz, M. A comparison of mechanism-inspired models for particle relative biological effectiveness (rbe). *Medical physics 45*, 11 (2018), e925–e952. 19

[130] Stützer, K., Lin, A., Kirk, M., and Lin, L. Superiority in robustness of multi-field optimization over single-field optimization for pencil-beam proton therapy for oropharynx carcinoma: an enhanced robustness analysis. *International Journal of Radiation Oncology* Biology* Physics 99*, 3 (2017), 738–749. 27

[131] Tessonnier, T., Böhlen, T., Ceruti, F., Ferrari, A., Sala, P., Brons, S., Haberer, T., Debus, J., Parodi, K., and Mairani, A. Dosimetric verification in water of a monte carlo treatment planning tool for proton, helium, carbon and oxygen ion beams at the heidelberg ion beam therapy center. *Physics in Medicine & Biology 62*, 16 (2017), 6579. 15, 23

[132] Tessonnier, T., Mairani, A., Brons, S., Haberer, T., Debus, J., and Parodi, K. Experimental dosimetric comparison of 1h, 4he, 12c and 16o scanned ion beams. *Physics in Medicine & Biology 62*, 10 (2017), 3958. 15

[133] Tessonnier, T., Marcelos, T., Mairani, A., Brons, S., and Parodi, K. Phase space generation for proton and carbon ion beams for external users' applications at the heidelberg ion therapy center. *Frontiers in oncology 5* (2016), 297. 27

[134] Tinganelli, W., and Durante, M. Carbon ion radiobiology. *Cancers 12*, 10 (2020), 3022. 77, 79, 82

[135] Tinganelli, W., Durante, M., Hirayama, R., Krämer, M., Maier, A., Kraft-Weyrather, W., Furusawa, Y., Friedrich, T., and Scifoni, E. Kill-painting of hypoxic tumours in charged particle therapy. *Scientific reports 5*, 1 (2015), 1–13. 25, 80

[136] Toma-Dasu, I., Dasu, A., Vestergaard, A., Witt Nyström, P., and Nyström, H. Rbe for proton radiation therapy–a nordic view in the international perspective. *Acta Oncologica 59*, 10 (2020), 1151–1156. 77

[137] Uhl, M., Mattke, M., Welzel, T., Roeder, F., Oelmann, J., Habl, G., Jensen, A., Ellerbrock, M., Jäkel, O., Haberer, T., et al. Highly effective treatment of skull base chordoma with carbon ion irradiation using a raster scan technique in 155 patients: first long-term results. *Cancer 120*, 21 (2014), 3410–3417. 80

[138] Unkelbach, J., Alber, M., Bangert, M., Bokrantz, R., Chan, T. C., Deasy, J. O., Fredriksson, A., Gorissen, B. L., Van Herk, M., Liu, W., et al. Robust radiotherapy planning. *Physics in Medicine & Biology 63*, 22 (2018), 22TR02. 2, 27

[139] Van Leeuwen, C., Oei, A., Crezee, J., Bel, A., Franken, N., Stalpers, L., and Kok, H. The alfa and beta of tumours: a review of parameters of the linear-quadratic model, derived from clinical radiotherapy studies. *Radiation oncology 13*, 1 (2018), 1–11. 3, 80

[140] Vavilov, P. Ionization losses of high-energy heavy particles. *Soviet Phys. JETP 5* (1957). 10

[141] Volz, L., Kelleter, L., Brons, S., Burigo, L., Graeff, C., Niebuhr, N., Radogna, R., Scheloske, S., Schömers, C., Jolly, S., et al. Experimental exploration of a mixed helium/carbon beam for online treatment monitoring in carbon ion beam therapy. *Physics in Medicine & Biology 65*, 5 (2020), 055002. 83

[142] Wan Chan Tseung, H., Ma, J., and Beltran, C. A fast gpu-based monte carlo simulation of proton transport with detailed modeling of nonelastic interactions. *Medical physics 42*, 6Part1 (2015), 2967–2978. 23, 78

[143] Weber, U., and Kraft, G. Design and construction of a ripple filter for a smoothed depth dose distribution in conformal particle therapy. *Physics in Medicine & Biology 44*, 11 (1999), 2765. 10

[144] Wedenberg, M., Lind, B. K., and Hårdemark, B. A model for the relative biological effectiveness of protons: the tissue specific parameter α/β of photons is a predictor for the sensitivity to let changes. *Acta oncologica 52*, 3 (2013), 580–588. 3, 7, 30, 79

[145] Widesott, L., Lorentini, S., Fracchiolla, F., Farace, P., and Schwarz, M. Improvements in pencil beam scanning proton therapy dose calculation accuracy in brain tumor cases with a commercial monte carlo algorithm. *Physics in Medicine & Biology 63*, 14 (2018), 145016. 2

[146] Wieser, H.-P., Cisternas, E., Wahl, N., Ulrich, S., Stadler, A., Mescher, H., Müller, L.-R., Klinge, T., Gabrys, H., Burigo, L., et al. Development of the open-source dose calculation and optimization toolkit matrad. *Medical physics 44*, 6 (2017), 2556–2568. 25, 77

[147] Wilkens, J., and Oelfke, U. A phenomenological model for the relative biological effectiveness in therapeutic proton beams. *Physics in Medicine & Biology 49*, 13 (2004), 2811. 6

[148] Wilson, R. R. Radiological use of fast protons. *Radiology 47*, 5 (1946), 487–491. 1

[149] Zhu, X. R., Li, Y., Mackin, D., Li, H., Poenisch, F., Lee, A. K., Mahajan, A., Frank, S. J., Gillin, M. T., Sahoo, N., et al. Towards effective and efficient patient-specific quality assurance for spot scanning proton therapy. *Cancers 7*, 2 (2015), 631–647. 2

Acknowledgements

First, I would like to thank **Prof. Dr. Dr. Jürgen Debus** for his supervision during the last years and the opportunity to write my thesis at the DKFZ, NCT, and HIT. Further, I would like to thank **Prof. Dr. Oliver Jäkel** for his engagement as a second reviewer.

I would like to express my deepest gratitude towards **PD Dr. Andrea Mairani** who above all was interested in my work and always sprouted of ideas. Thank you very much for taking me into the BioPT group, I really learned a lot.

I would also like to thank **Assist. Prof. Dr. Amir Abdollahi** for his insightful comments and for enabling so many of my projects. A heartful thanks to **Prof. Dr. Thomas Haberer** for giving me the opportunity to carry out my thesis at HIT. A big thank you also to **Prof. Dr. Markus Alber** for supporting me in the early stages of the thesis and enabling my exchange with the DCPT.

A big thanks also to **Dr. Ivana Dokic** and the whole **E210/E050** team. To the colleagues at HIT, **Dr. Stephan Brons**, **Dr. Semi Ben Harrabi**, **Swantje Ecker**, **Dr. Christian Schömers**, **Timo Strecker**, and **Dr. Julia Bauer** and everyone I forgot to mention here also thank you. A big thank you to **Maria Fuglsang Jensen** and her colleagues at DCPT for hosting me in Aarhus.

Furthermore, I would like to thank my BioPT group members: **Mac**, **Judith**, **Hans**, **Friderike**, **Nish**, **Peter**, **Ozan**, and last but not least **Thomas**.
Thank you for sharing these last years with me. I will never forget them.

All my love to my **family** and **friends** who always helped and supported me.

Josefine thank you for everything! Without you, I would not have made it to this point!

Erklärung

Ich erkläre hiermit, dass ich die vorgelegte Dissertation selbst verfasst und mich dabei keiner anderen, als der von mir ausdrücklich bezeichneten Quellen und Hilfen bedient habe.

Heidelberg, den 29.01.2021

.....

Nanos gigantum humeris insidentes.